Metabolomics Effects of Folding Correction in Retinitis Pigmentosa Rhodopsin Mutant P23A

Metabolomics Effects of Folding Correction in Retinitis Pigmentosa Rhodopsin Mutant P23A

Meghana Hosahalli Shivananda Murthy[1] | Hannah Staggs-Sandy[2,3] | Paniz Jasbi[4] | Philip J. Reeves[2] | Judith Klein-Seetharaman[1,4,5]

[1]School of Molecular Sciences, Arizona State University, Tempe, Arizona, USA | [2]School of Life Sciences, University of Essex, Colchester, UK | [3]Norwich Medical School, University of East Anglia, Norwich, UK | [4]Systems Precision Engineering and Advanced Research (SPEAR), Theriome Inc., Phoenix, Arizona, USA | [5]College of Health Solutions, Arizona State University, Phoenix, Arizona, USA

Correspondence: Judith Klein-Seetharaman (jkleinse@asu.edu)

ABSTRACT

Retinitis pigmentosa (RP) is a hereditary retinal degeneration disorder often caused by mutations in the rhodopsin gene, leading to photoreceptor death and vision loss. While structural misfolding of rhodopsin is a known contributor to disease pathology, the mechanisms of its cellular and in particular metabolic consequences are poorly understood. To study the direct effects of rhodopsin misfolding and structural rescue on cellular metabolism, we used the P23A mutant and its N2C/D282C stabilized counterpart as a structural tool to assess how differences in folding stability relate to measurable changes at the metabolite level. The engineered cysteine pair allows the formation of a disulfide bond restoring structural integrity and reinforcing the stable seven-transmembrane bundle. We used untargeted Gas Chromatography–Mass Spectrometry (GC–MS) metabolomics analysis conducted in inducible rhodopsin-expressing cell lines, providing a broad and general profiling of metabolic pathway alterations in response to the expression of RP mutants and their structurally rescued counterparts. Principal component analysis, hierarchical clustering, and *K*-means clustering revealed distinct metabolic signatures associated with each rhodopsin-expressing cell line, demonstrating a highly significant effect of genotype on global metabolite composition ($F = 71.679$; $R^2 = 0.93724$; $p = 0.001$). Pairwise comparisons and background-subtracted analyses identified consistent alterations in arginine and proline metabolism, glutathione metabolism, and the TCA cycle, nucleotide, amino acid metabolism, redox regulation, and mitochondrial function in cells expressing misfolded P23A. Pathway enrichment highlighted key metabolites in the respective pathways as candidate biomarkers for the rhodopsin P23A mutation. As this study employs a non-retinal cell system, the observed metabolic changes reflect conserved responses to rhodopsin misfolding and proteostatic stress in the ER rather than a direct model of rod cell degeneration. Our findings support the hypothesis that there is a biochemical link, most likely the UPR, between rhodopsin folding/misfolding status and metabolic homeostasis and suggest that targeted metabolic modulation may offer a complementary therapeutic avenue for treating RP.

1 | Introduction

Retinitis pigmentosa (RP) is a group of inherited retinal degenerative diseases in which photoreceptor cells die causing progressively deteriorating vision starting with night blindness, tunnel vision, and resulting eventually in some cases in complete blindness [1]. RP symptoms often arise as early as when patients are 10–20 years old, affecting over 2 million people worldwide aged less than 60 years old [1, 2]. The prevalence of RP is estimated to be about 1:3000 [1]. Currently, there is no cure. RP is caused by more than 3000 individual mutations in 80 genes [3]. Autosomal dominant retinitis pigmentosa (adRP) accounts for 20%–25% of all inherited

RP cases [1], involving mutations in more than 25 genes. Of these, the rhodopsin gene alone accounts for over 150 distinct mutations, representing the most common cause [4–6].

Rhodopsin is a light-sensitive G protein-coupled receptor (GPCR) embedded in the disc membranes in the rod outer segment [7]. It functions as the primary molecular sensor of light, initiating the phototransduction cascade that converts photon signals into electrical impulses transmitted to the brain [7]. Structurally, rhodopsin is composed of seven transmembrane α-helices that divide the protein into an extracellular domain, a transmembrane domain and an intracellular domain containing three loops on each side, as shown in Figure 1. A single polypeptide chain of 348 amino acids, the apo-protein opsin folds into a helical bundle that provides a pocket for binding *11-cis*-retinal which is covalently linked to K296 [7, 8]. Upon light absorption, the *11-cis*-retinal chromophore undergoes isomerization to *all-trans*-retinal, causing a conformational change in the protein. This activated state, Metarhodopsin II, catalyzes the activation of the G protein transducin, triggering downstream signaling that results in hyperpolarization of the photoreceptor cell [8]. Rhodopsin's correct folding, trafficking to the outer segment, and stability are essential for photoreceptor function [9].

Two major classes of rhodopsin-associated adRP mutations have been shown to impair folding, leading to mislocalization, aggregation, and activation of cellular stress pathways [4, 9]. Class I mutations for example, R135G, R135L, R135W, V345L, and P347L, cause severe, early-onset degeneration characterized by global loss of rod function and early night blindness, reflecting irreversible rod damage. Class II mutations for example, T17M, P23A/H/L, T58R, V87D, G106R, D190G, G51A, Q64ter, and Q344ter produce a milder phenotype, with largely preserved rod activation kinetics and outer segment structure but with mutation-specific defects in the visual cycle [1–5]. Because rods in the Class II group remain viable, their preservation is a key therapeutic goal. The P23H variant is the most prevalent adRP mutation in North America, accounting for approximately 10% of cases due to a founder effect [9, 10]. The replacement of H by A, also a class II variant, results in an even milder phenotype. Both P23H and P23A mutations cause protein misfolding, instability, and endoplasmic reticulum (ER) retention, triggering the unfolded protein response (UPR), disrupting proteostasis, and promoting photoreceptor cell death, a hallmark of RP progression [4, 6]. This cellular phenotype can be prevented in vitro in rhodopsin-expressing cells [11] treated with pharmacological chaperones such as *11-cis*-retinal or *9-cis*-retinal [7]. Such treatments can reverse the RP mutant phenotype and can partially restore folding and rhodopsin formation [7–9]. However, despite improved expression, the thermal stability and functionality of mutant pigments remain affected [5]. To overcome this limitation, a structurally stabilized rhodopsin variant N2C/D282C has been developed to restore N-terminal integrity and reinforce the seven-transmembrane bundle [4, 5]. The engineered cysteine pair N2C/D282C allows the formation of a stabilizing disulfide bond between the two introduced cysteines, as shown in Figure 1. The disulfide linkage enhances the thermostability of rod opsin and facilitates the structural recovery of misfolded variants [5], providing a robust platform for investigating folding dynamics and rescue mechanisms in Class II rhodopsin mutations [5]. Although less extensively studied than P23H, P23A was chosen for the present study due to its higher responsiveness to the N2C/D282C structural correction [5], which promotes proper folding and trafficking, thereby serving as a useful model for exploring therapeutic rescue of misfolded rhodopsin [6, 9].

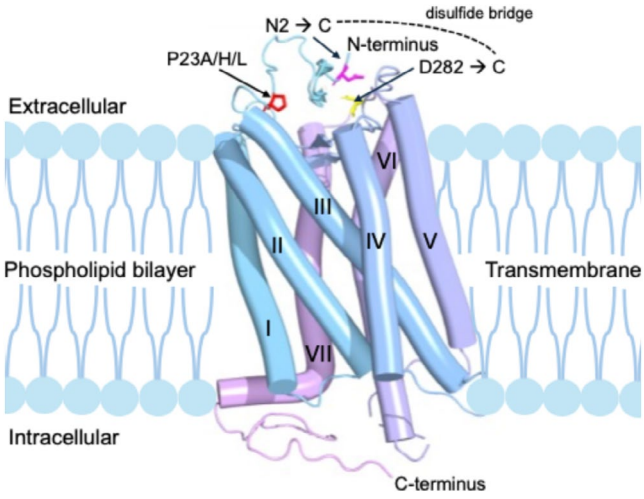

FIGURE 1 | Structural representation of rhodopsin highlighting the P23A mutation and N2C/D282C disulfide bond correction strategy. Rhodopsin, a prototypical GPCR, is composed of seven transmembrane α-helices (I–VII), dividing the protein into extracellular, transmembrane, and intracellular regions. The figure illustrates the helical topology and loop architecture characteristic of rhodopsin. P23A/H/L substitutions are located in the extracellular N-terminal region (red). These substitutions are so-called class II mutations, characterized by causing protein misfolding and ER retention. The engineered N2C/D282C substitutions (marked in pink and yellow, respectively) form a stabilizing intramolecular disulfide bridge that structurally corrects the misfolding caused by the mutation at position P23.

Recent studies show that rhodopsin RP mutations cause not only protein misfolding but also metabolic dysfunction, including impaired oxidative phosphorylation, AMPK activation, and glycolytic reprogramming, offering new explanations for variability in disease severity [10]. The retina is highly metabolically active, with rods comprising ~95% of photoreceptors and relying on tight metabolic coupling with the retinal pigment epithelium (RPE) [11, 12]. Oxidative stress contributes to degeneration, and the loss of rods leads to excess retinal oxygen and secondary cone death [13–18]. Microarray analyses revealed that approximately one-third of genes altered during retinal degeneration are involved in metabolism, highlighting the central role of metabolic regulation in photoreceptor survival [19]. The insulin/mTOR signaling pathway, classically associated with nutrient sensing, glucose uptake, glycolysis, protein and nucleotide synthesis, and *de novo* lipogenesis, is repeatedly implicated in RP progression [12, 19–22], as are metabolic disorders with retinal involvement, such as Refsum disease and diabetic retinopathy [23]. The metabolic nature of RP is further supported by findings that the antidiabetic drug metformin modulates RP progression, likely through AMPK-mediated mechanisms [24, 25]. According to the metabolic coupling hypothesis, the RPE normally provides glucose to photoreceptors [19], which convert it into lipids and lactate to sustain outer segment renewal, while the RPE uses lactate as its carbon source [26]. In RP, reduced lipid and lactate levels disrupt this balance, causing the RPE to consume glucose

instead, depriving photoreceptors of energy and driving a vicious cycle of metabolic failure and cell death [27, 28].

Understanding and restoring this metabolic coupling is therefore critical to mitigating photoreceptor degeneration. To address this need, recent metabolomic profiling of RP animal models has been carried out, which revealed perturbations in oxidative stress responses and mitochondrial metabolism [29]. Weiss et al. conducted a metabolomic analysis in the rd10 mouse model of retinal degeneration, identifying alterations in the TCA cycle, fatty acid oxidation, and purine metabolism during photoreceptor cell loss [29]. Liu et al. utilized Seahorse extracellular flux analysis to measure oxygen consumption and glycolytic rates in 661w cells and reported that overexpression of rhodopsin mutants, including WT and P23H, leads to oxidative phosphorylation deficiency as a result of mitochondrial loss and increased glycolytic dependence, contributing to bioenergetic stress and cell damage [10]. Recent large-scale proteomic analysis of different RP mouse models, including the P23H mouse, has revealed that despite distinct genetic mutations, concurrent disruptions occur across core metabolic and signaling pathways [30]. However, there is a critical gap in our understanding of how rhodopsin misfolding is connected to cellular bioenergetics and metabolism.

While RP is a retina-specific disease, isolating the direct cellular consequences of rhodopsin misfolding in native retinal systems remains challenging due to the complexity of phototransduction, chromophore cycling, and metabolic coupling between photoreceptors and the RPE. To address this, we employed a tetracycline-inducible HEK293S stable cell system, which has been extensively used to study rhodopsin folding, ER retention, and structural rescue of class II mutants in a controlled environment [5, 6]. This system enables regulated expression of opsin independent of retinal-specific processes, allowing direct interrogation of proteostasis-driven cellular responses to misfolded rhodopsin. We note that this model does not recapitulate photoreceptor-specific metabolism, the visual cycle, or RPE–photoreceptor metabolic coupling. Therefore, the metabolic changes observed in this study reflect conserved cellular responses to rhodopsin misfolding and proteostatic stress at the ER rather than a direct model of retinal degeneration. However, we consider our results highly relevant because in both rod cells and HEK293S model cells, the site of stress is the same.

To study the direct effects of rhodopsin misfolding and structural rescue on cellular metabolism, we used the P23A mutant and its N2C/D282C stabilized counterpart as a structural tool to assess how differences in folding stability relate to measurable changes at the metabolite level. We hypothesize that metabolic dysfunction arising from rhodopsin misfolding constitutes a key mechanistic link between protein instability and photoreceptor degeneration in RP. The present study represents the first untargeted Gas Chromatography–Mass Spectrometry (GC–MS) metabolomics analysis conducted in inducible rhodopsin-expressing cell lines with rhodopsin mutation, providing a broad and general profiling of metabolic pathway alterations in response to the expression of RP mutants and their rescued counterparts. Since rhodopsin is likely bound to retinal chromophore in many in vivo models, it is difficult to differentiate between retinal binding and misfolding. Inducible cell lines used in this study circumvent this limitation, enabling direct observation of metabolic changes from the misfolded opsin apoprotein alone, free from chromophore interference [5, 6]. Using wild type (WT), P23A, and the structurally stabilized P23A/N2C/D282C rhodopsin-expressing variant, we explored the metabolomic profiles of misfolded rhodopsin and its structural correction to identify key metabolites and metabolic pathways associated with rhodopsin misfolding and cellular stress responses relevant to RP.

2 | Methods

2.1 | Materials and Reagents

Dulbecco's modified Eagle's medium (DMEM) (Cat. No. 12100061), Fetal bovine serum (FBS) (Cat. No. MT35010AC22), Penicillin–Streptomycin (Pen-Strep, 10000 U/mL) (Cat. No. 15140122), 10× Phosphate-Buffered Saline (PBS) (Cat. No. BP3994), Methanol (MeOH) (Cat. No. A454-4), Pyridine > 99% (Cat. No. P368), Methoxamine hydrochloride > 98% (MeOX) (Cat. No. AC2104490050), Methyl tert-butyl ether > 99% (MTBE) (Cat. No. E127-4), Restore Western Blot stripping buffer (Cat. No. PI21059), Tris Base > 99.8% (Cat. No BP152), Glycine 99% (Cat. No. AAA138160E), NaCl (Cat. No. BP358-10), Halt Protease and Phosphatase Inhibitor (Cat. No. PI78442), Secondary Anti-rabbit antibody (Cat. No. 32460), Gibco Trypsin–EDTA (Cat. No. 25200056), Tetracycline Hydrochloride (TAC) (Cat. No. BP912), and sodium butyrate (NaBu) (Cat. No. AAA1107906) were purchased from Fisher Scientific. RIPA lysis buffer (Cat. No. R0278), N-(tert-butyldimethylsily)l-N-methyltrifluoroacetamide (MTBSTFA) (Cat. No. 77626), and Myristic-d27 acid (Cat. No. 366889) were purchased from Sigma. RHO 1D4 antibody (UBC Flintbox), SDS Micro-pellets (VMR, Cat. No. 76346-472), GAPDH antibody (Cell Signaling, Cat. No. 97166S). Protein molecular weight marker (Cat. No. 1610374), 4%–20% Mini PROTEAN TGX precast protein gel (Cat. No. 4561094), and 2× Laemmli Sample Buffer (Cat. No. 1610737) were purchased from Bio-Rad. Blocking Buffer (Cat. No. AC2148), Low Fluorescence Western membrane (PVDF) (Cat. No. AC2105), and Radiance Plus Chemiluminescent substrate (Cat. No. AC2103) were purchased from Azure Biosystems. 1,2-Diheptadecanoyl-sn-Glycero-3-Phosphatidylcholine (17:0, PC) (Cat. No. A85360) and 1,2-diheptadecanoyl-sn-glycero-3-phospho-(1′-rac-glycerol) (17:0, PG) (Cat. No. A83456) were purchased from Avanti Research.

2.2 | Cell Lines and Growth Conditions

Stable Human embryonic kidney 293S-GnTI- TetR (HEK 293S-GnTI- TetR) with tetracycline-inducible opsin cell lines (WT, P23A, and P23A/N2C/D282C) were constructed by integration of a cassette containing CMVtetO regulated opsin genes, University of Essex, England [4]. The stable cell lines represent pools of cells with random insertions of the expression cassette generated by a transposon delivery system which likely increases the frequency of insertions without revealing chromosomal position. Cells were cultured in cell culture media containing DMEM with high glucose supplemented with 10% FBS and 1% pen-strep at 37°C in a 5% CO_2 incubator. In all of the experiments, the cells were harvested after 24 h of

induction with tetracycline (TAC) (2 μg/mL) and sodium butyrate (NaBu) (5 mM) [5, 6].

2.3 | Cell Culture and Treatment Conditions

Frozen HEK293S cell pellets were thawed in a water bath at 37°C for 2 min, diluted slowly in 10 mL of fresh medium, then centrifuged at 1000 rpm for 2 min. The supernatant was aspirated, and the cell pellet was gently resuspended in 10 mL of DMEM containing high glucose (Invitrogen) supplemented with 10% FBS and 1% pen-strep and transferred to 10 cm cell culture dish. The cells were grown in a 10 cm cell culture dish and maintained till confluency. Media was aspirated, the plate containing cells was rinsed with PBS and 2 mL trypsin was added to the dish. Cells were trypsinized for 5 min at 37°C in a 5% CO_2 incubator. 6 mL of cell culture media was added to neutralize trypsinization, and cells were collected in a 10 mL centrifuge tube. Cells were spun at 4000 rpm for 5 min, aspirated supernatant, and resuspended pellets in 1 mL cell culture media. 10 μL of cell suspension was mixed with 10 μL of trypan blue, and 10 μL of cells with trypan blue mixture was added to the hemocytometer, and cells were counted in EVE Automated Cell Counter (NanoEnTek). A cell density of 0.5×10^6 per well was added into 6-well plates, maintained in 2 mL cell culture media at 37°C in a 5% CO_2 incubator. After reaching 70% confluency, plates were induced with 1 mL cell culture media containing tetracycline and sodium butyrate and harvested after 24 h.

Opsin cell lines stably transfected with WT, P23A mutant, or P23A/N2C/D282C opsin genes were treated with an induction cocktail containing cell culture medium with tetracycline and sodium butyrate (TAC/NaBu) and without TAC/NaBu in 6-well plates with replicates of 5 wells for metabolomics and 3 wells for western blot analysis. Cells were treated as follows: control without any treatments, 2 μg/mL tetracycline (TAC) only, 5 mM sodium butyrate only (NaBu), with TAC/NaBu. Cells were harvested 24 h after treatment by scraping the wells and collecting the cell suspension in 1 mL Eppendorf tubes for metabolomics and Western blot analysis. These experiments were carried out in three different independent batches summarized in Table 1.

2.4 | Cell Viability Assay

Cell viability was assessed using the EVE Automated Cell Counter (NanoEnTek). A 1:1 mixture of cell suspension and trypan blue was prepared by combining 10 μL of cell suspension with 10 μL of dye and incubating the mixture for 3–5 min at room temperature to allow selective staining of non-viable cells. Following incubation, 10 μL of the stained cell mixture was loaded into an EVE disposable counting slide, and viable cell numbers were recorded using the automated counting program according to the manufacturer's instructions. The instrument-reported viable cell count was used directly for downstream normalization.

2.5 | SDS PAGE and Western Blot Analysis

Cells were pelleted by centrifugation at 4000 rpm for 5 min, and the supernatant was aspirated. Approximately 1×10^6 cells were collected and was lysed in a RIPA buffer containing Protease and Phosphatase Inhibitor, vortexed for 30 s, and placed on ice for 10 min. The lysate was mixed with 1× Laemmli sample buffer and boiled at 90°C for 10 min. Whole-cell lysates were spun down, and the protein lysate supernatant was collected in a separate Eppendorf tube. Protein samples were run on Biorad's 4%–20% Mini PROTEAN TGX precast protein gels in a running buffer (150 mM Tris base, 190 mM glycine, and 0.1% SDS) at 120V for 90 min.

Following electrophoresis, proteins were transferred onto PVDF membranes by complete immersion of the gel–membrane sandwich in transfer buffer (25 mM Tris base, 190 mM glycine, and 20% methanol) at 0.33 Amps for 90 min. PVDF membranes were preactivated with methanol for 1 min before transfer to ensure efficient protein binding. After transfer, membranes were blocked in blocking buffer (Azure Biosystems) for 1 h at room temperature. Membranes were washed three times with washing buffer (1× Tris-buffered saline with Tween-20) and incubated overnight at 4°C with RHO 1D4 antibody (rabbit, 1:10000) to detect rhodopsin. Following incubation, membranes were washed and incubated with HRP-conjugated anti-rabbit secondary antibody (1:5000) for 2 h at room temperature. The blots were developed using Radiance Plus chemiluminescent substrate (Bio-Rad) for 5 min, and protein bands were visualized using a Bio-Rad imaging system. Membranes were then stripped using Restore Western blot stripping buffer (Fisher Scientific) and reprobed with GAPDH antibody (rabbit, 1:1000) followed by HRP-conjugated secondary antibody (1:5000) for normalization of protein loading. The mean intensity of the protein bands was quantified using ImageJ software.

2.6 | Gas Chromatography–Mass Spectrometry (GC–MS) Sample Preparation

The sample preparation protocol was adopted from previous studies [31, 32]. The cell suspension containing 10^6 cells was combined with 200 μL of 10× diluted PBS and 80 μL of MeOH supplemented with 50 μM PC (17:0, 17:0) and PG (17:0, 17:0) internal standards. Although these are lipid standards, they were

TABLE 1 | Overview of the number of experimental groups and replicates.

Experiments	Replicates	Cells	Treatments
E1	5	P23A; P23A/N2C/D282C	Tac/NaBu
E2	5	WT; P23A; P23A/N2C/D282C	Tac/NaBu
E3	5	P23A; HEK293	Tac/NaBu; Tac; NaBu

included solely as process-monitoring controls to assess extraction consistency; quantification of aqueous metabolites was performed using internal standard ratios and reported as relative abundances. The mixture was vortexed for 30 s, followed by the addition of 400 μL of MTBE (MTBE:MeOH:H_2O = 10:2.5:2, v/v/v). Samples were then stored at −20°C for 20 min and centrifuged at 22 000 g for 10 min at 4°C to facilitate phase separation. Subsequently, 180 μL of the aqueous (bottom) layer was carefully collected and transferred to a new Eppendorf tube for derivatization.

The collected samples were dried under vacuum at 37°C for 4 h using a vacuum concentrator/evaporator and reconstituted in 40 μL of methoxyamine hydrochloride in pyridine (20 mg mL^{-1}). The reconstituted samples were incubated at 60°C for 90 min. Following this step, 60 μL of MTBSTFA was added, and the samples were incubated again at 60°C for 30 min. The resulting mixture was vortexed for 30 s and centrifuged at 22 000 g for 10 min. Finally, 70 μL of the supernatant was collected from each sample for GC–MS analysis.

GC–MS analysis was performed under conditions adapted from previous studies [33, 34]. Briefly, a 2 μL aliquot of each prepared sample was injected into an Agilent 7820A GC-5977B MSD system (Santa Clara, CA). Helium served as the carrier gas with a constant flow rate of 1.2 mL min^{-1}. Metabolites were separated using an Agilent HP-5 ms capillary column (30 m × 250 μm × 0.25 μm). The column temperature was held at 60°C for 1 min, ramped at 10°C min^{-1} to 325°C, where it was held for 10 min. Mass spectra were acquired across an m/z range of 60–500 following a 3 min solvent delay.

Data extraction was performed using Agilent MassHunter Quantitative Analysis software (version B.07.00). A batch recursive feature extraction workflow optimized for small molecules was applied, and only peaks with an absolute height ≥ 1000 counts were retained. The dataset included blanks to monitor carryover and contamination, and all injections were randomized to minimize run-order effects. Signal drift across the batch was evaluated using pooled QC samples injected periodically, and drift correction was applied when necessary. Metabolites were retained only if they exhibited a QC coefficient of variation (CV) < 20%, where CV was calculated from the pooled QC replicates, and if their relative abundance was ≥ 1000 in at least 80% of study samples.

2.7 | Metabolite Identification

Metabolite identification was performed against an in-house spectral library of 126 authentic chemical standards analyzed under identical GC–MS conditions, with all identifications meeting Metabolomics Standards Initiative (MSI) Level 1 criteria [35], namely co-elution with the authentic standard within ±0.05 min and matching quantifier and qualifier ion ratios within ±20%. The complete library, including compound name, KEGG identifier, HMDB identifier, retention time, quantifier m/z, qualifier ion(s), and MSI confidence level for each entry, is provided as Table S1. Raw GC–MS data files, sample metadata, and the spectral library have been deposited to the NIH Metabolomics Workbench [36].

2.8 | Data Analysis

Untargeted metabolomics analysis was performed using MetaboAnalyst 5.0, which provides integrated modules for data quality assessment, normalization, statistical testing, and pathway interpretation [37–39]. Within MetaboAnalyst, data integrity checks were performed to ensure consistent sample names, metabolite completeness, and the absence of missing metadata. Values below detection limits were imputed using one-half of the minimum positive value per metabolite. Intensities were then $\log_{10}$-transformed to stabilize variance and improve normality. Row-wise normalization was performed, in which GAPDH band intensity obtained from Western blot analysis and viable cell counts from cell viability assay were used as the reference to scale all other samples. Column-wise Pareto scaling [40] was applied to reduce the dominance of high-abundance metabolites while maintaining comparability across features.

An exploratory analysis was conducted using Principal Component Analysis (PCA) within the Statistical Analysis PCA module, with unit-variance scaling applied for visualization, allowing assessment of sample clustering, batch behavior, and potential outliers. Group-wise statistical comparisons were assessed using a one-way ANOVA with a between-groups design (three levels: WT, P23A, and P23A/N2C/D282C). Significant ANOVA findings were followed by post hoc pairwise Student's *t*-tests using MetaboAnalyst's default settings, and *p*-values were corrected using the Benjamini–Hochberg false discovery rate (FDR) method [41]. For exploratory interpretation in this untargeted context, metabolites with raw $p < 0.05$ were considered nominally significant; FDR values were computed using the Benjamini–Hochberg procedure across all detected metabolites. In this dataset, most metabolites yielded FDR values approaching 1 owing to the moderate sample size and the broadly correlated nature of the metabolite features under coordinated UPR and redox-driven remodeling. Therefore, no FDR-based filtering was applied, and all detected metabolites were retained for downstream multivariate analyses (PCA, PLS-DA, hierarchical clustering, and pathway enrichment), which do not require per-feature significance thresholding and are appropriate for hypothesis-generating untargeted metabolomic datasets of this scale [42, 43]. Fold-change values accompanied all statistical tests, and significant results were visualized using volcano plots, ANOVA summary tables, and significance scatter plots.

Supervised multivariate modeling [40] was used to identify combinations of metabolites that discriminated between the three rhodopsin-expressing cell lines. Partial least squares–discriminant analysis (PLS-DA) and Principal component analysis (PCA) were performed using the Statistical Analysis. PCA module with PERMANOVA (999 permutations) testing using MetaboAnalyst's default settings to evaluate model robustness and prevent overfitting, and to validate group separation across genotypes. PCA was used as an unsupervised approach to visualize intrinsic metabolomic variation. PLS-DA was performed to identify metabolites that most strongly contributed to group separation, and Variable Importance in Projection (VIP) scores were calculated to determine the key discriminating metabolites. Variable importance in VIP

scores [44] were calculated from the first component to rank discriminative metabolites. Cluster heatmaps and *K*-means clustering were generated to visualize co-regulated metabolite groups and group-specific metabolic signatures. To address technical variation across the three experimental batches, batch-effect correction was applied using the empirical Bayes ComBat algorithm [45] to remove batch-related variation without altering biological signals.

Pathway-level interpretation was performed using the Functional Analysis suite in MetaboAnalyst. Metabolite Set Enrichment Analysis (MSEA) employed the SMPDB library [46, 47] with over-representation analysis (ORA), which evaluates whether significantly altered metabolites occur more frequently than expected by chance within predefined biochemical pathways [48]. Pathway-level perturbations were inferred using the MS Peaks-to-Pathways workflow (mummichog v2.0 [49] combined with Gene Set Enrichment Analysis [50, 51]), implemented with human KEGG pathways [52, 53]. This approach enabled the identification of pathway-level alterations associated with rhodopsin misfolding and structural rescue. This integrated workflow enabled metabolite-level and pathway-level interpretation of metabolic differences across WT, P23A, and P23A/N2C/D282C cell lines.

3 | Results

3.1 | Experimental Setup

Experimental studies of rhodopsin misfolding require a robust and tightly controllable expression system to distinguish folding-dependent effects from background cellular metabolism. To this end, we employed a modified version of the previously established tetracycline-inducible HEK293S-GnTI$^-$ to generate stable cell line pools of cells expressing WT rhodopsin, the misfolded P23A mutant, and the structurally stabilized P23A/N2C/D282C variant [6]. This inducible system enables regulated opsin expression with minimal basal leakiness, while combined treatment with tetracycline and sodium butyrate (TAC/NaBu) enhances rhodopsin yield without compromising cell viability. Importantly, these stable lines recapitulate known folding and trafficking behaviors of rhodopsin in a controlled cellular environment, allowing direct comparison between WT and RP mutant constructs. As a non-retinal system, however, this model does not capture photoreceptor-specific metabolism or visual cycle processes and is therefore used here to isolate folding- and proteostasis-associated cellular responses to rhodopsin misfolding, which is the same in both cell types.

Using this system, three independent experiments were designed to systematically isolate metabolic changes associated with rhodopsin misfolding while controlling for reagent- and cell line–specific effects (Table 1). Each experiment contained five biological replicates per condition. Experiment 1 (E1) examined P23A and P23A/N2C/D282C under TAC/NaBu induction to assess the impact of structural stabilization. Experiment 2 (E2) included WT, P23A, and P23A/N2C/D282C under the same TAC/NaBu condition, enabling direct comparison of metabolic profiles across all three rhodopsin constructs. Experiment 3 (E3) compared P23A with HEK293 empty vector controls (HEK293) under TAC/NaBu, TAC-only, and NaBu-only treatments to isolate reagent and cell line–specific metabolic effects. This design ensured that metabolic signatures attributed to misfolded rhodopsin were not confounded by induction reagents or background cellular metabolism.

3.2 | Rhodopsin Expression Is Reliably Induced Across Three Independent Experiments

Western blot analysis across the three experiments confirmed reliable inducible expression of rhodopsin by TAC/NaBu (Figure 2). Untreated samples showed no rhodopsin bands, confirming the requirement of TAC/NaBu for rhodopsin expression. TAC/NaBu-treated samples showed characteristic diffuse rhodopsin banding patterns in cell lines expressing WT, P23A, and P23A/N2C/D282C (Figure 2A,B), as expected due to heterogeneous glycosylation [6]. WT and P23A/N2C/D282C samples exhibited similar diffuse banding patterns. In contrast, the P23A mutant showed altered band intensity and differences in band distribution relative to WT and P23A/N2C/D282C. HEK293 empty cells showed no signal under any condition, confirming antibody specificity (Figure 2C). Furthermore, Anti-GAPDH blotting confirmed equal protein loading across all samples (Figure 2). As samples were denatured prior to electrophoresis, these analyses were used to assess inducible rhodopsin expression and relative expression patterns rather than directly evaluating folding status.

3.3 | Distinct Clustering of WT, P23A and Structurally Rescued P23A/N2C/D282C Metabolite Profiles

To assess whether rhodopsin folding drives global differences in metabolic profiles, batch-corrected metabolomic data were analyzed by principal component analysis (PCA) (Figure 3). PCA provides an overview of global metabolic variance. Across all experiments (Figure 3A), P23A TAC/NaBu cells formed a distinct cluster along PC1, separating clearly from WT and P23A/N2C/D282C, indicating a unique metabolic signature associated with misfolded rhodopsin. WT and P23A/N2C/D282C cells, both untreated and TAC/NaBu treated, clustered closely, demonstrating that structural correction restores a WT-like metabolic profile. HEK293 controls and P23A untreated samples showed partial overlap, consistent with treatment and cell-line–dependent background variation. Biological replicates clustered tightly, confirming data reliability across all five biological replicates.

Individual experimental analyses further supported these trends. In E1 and E2 (Figure 3B), P23A TAC/NaBu samples again separated from WT and P23A/N2C/D282C, whereas P23A/N2C/D282C TAC/NaBu samples shifted toward the WT TAC/NaBu cluster. Untreated and TAC/NaBu-P23A were clustered in different regions of the plot. E3 (Figure 3C) demonstrated that P23A TAC/NaBu cells also clustered away from HEK293 controls, while HEK293 TAC/NaBu and untreated conditions overlapped, confirming that TAC and NaBu do not substantially alter the metabolic profile of cells lacking

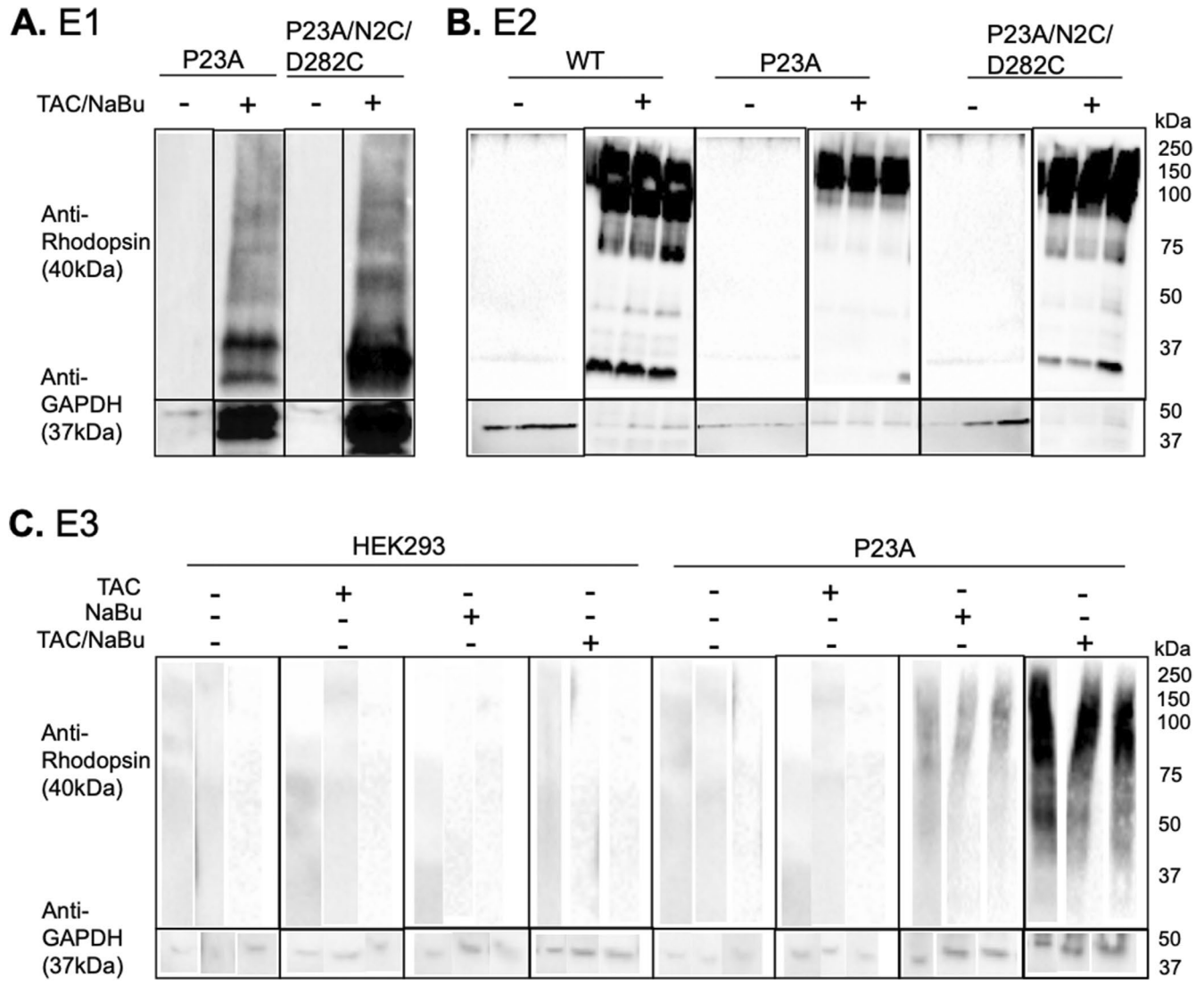

FIGURE 2 | Inducible expression of rhodopsin across experimental conditions. Western blot analysis of rhodopsin expression using anti-1D4 antibody, with GAPDH as a loading control, across three independent experiments (E1–E3; see Table 1). (A) Experiment 1 (E1): P23A and P23A/N2C/D282C cells treated with TAC/NaBu. (B) Experiment 2 (E2): WT, P23A, and P23A/N2C/D282C cells treated with TAC/NaBu. (C) Experiment 3 (E3): HEK293 empty vector and P23A cells treated with TAC only, NaBu only, or TAC/NaBu. Diffuse rhodopsin bands are observed only in TAC/NaBu-treated samples, confirming inducible expression. WT and P23A/N2C/D282C exhibit comparable band patterns, whereas P23A shows altered intensity consistent with misfolding.

rhodopsin and mainly function as an inducer in rhodopsin-expressing cell lines. To evaluate the robustness of group separation observed in the metabolomic analyses, we performed a PERMANOVA test with 999 permutations (see Methods). The P23A induced state was the most distinct, showing highly significant separation from both the P23A/N2C/D282C TAC/NaBu ($F = 124.78$; $R^2 = 0.93975$; $p.\text{adj} = 0.013$) and WT TAC/NaBu groups ($F = 74.30$; $R^2 = 0.90279$; $p.\text{adj} = 0.013$). The results demonstrated a highly significant effect of genotype on global metabolite composition ($F = 71.679$; $R^2 = 0.93724$; $p = 0.001$), with high F-values and R^2 indicating that 93.7% of the variance in the dataset is explained by differences among WT, P23A, and P23A/N2C/D282C groups. The comparison between P23A/N2C/D282C induced and WT induced showed a lower but still significant separation ($F = 9.81$; $R^2 = 0.55078$; $p.\text{adj} = 0.013$), indicating that although structural correction shifts the metabolic profile toward WT. The low permutation-based p-value confirms that the observed clustering is not attributable to random variation. These results provide strong statistical support for the distinct metabolic profiles identified in the PCA. To link these global patterns to specific metabolic changes, key metabolites identified through VIP analysis and differential comparisons were examined. Metabolites such as L-arginine, L-glutamic acid, pyroglutamic acid, methylmalonic acid, and cyclic AMP consistently contributed to group-level differences across analyses. These metabolites are central to amino acid metabolism, redox balance, and mitochondrial function, indicating that the observed global separation is primarily driven by coordinated perturbations in these core metabolic pathways rather than diffuse changes across the metabolome. Collectively, these PERMANOVA results support that misfolded P23A rhodopsin produces the most divergent metabolic signature, while the structurally corrected P23A/N2C/D282C variant exhibits a partially restored, intermediate metabolic state.

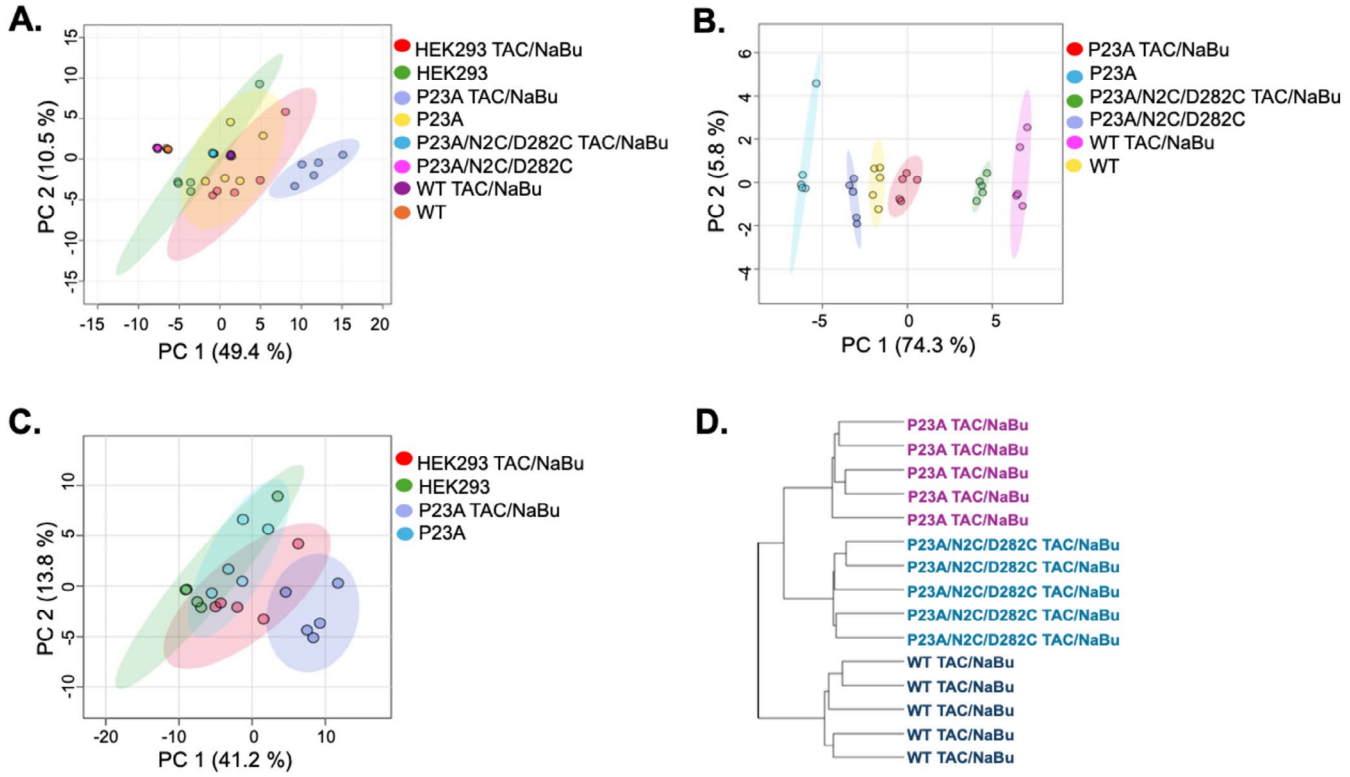

FIGURE 3 | Global metabolomic patterns across rhodopsin constructs. Principal component analysis (PCA) and hierarchical clustering of batch-corrected metabolomic data. (A) PCA of all experiments (E1–E3) showing distribution of WT, P23A, and P23A/N2C/D282C samples. (B) PCA of E1 and E2 highlighting TAC/NaBu-treated WT, P23A, and P23A/N2C/D282C conditions. (C) PCA of E3 comparing P23A with HEK293 controls under different treatment conditions. (D) Hierarchical clustering dendrogram of TAC/NaBu-treated WT, P23A, and P23A/N2C/D282C samples ($n = 5$ biological replicates). P23A samples exhibit a distinct metabolic profile, while P23A/N2C/D282C samples display an intermediate profile relative to WT.

Hierarchical clustering (Figure 3C) recapitulated PCA results: P23A TAC/NaBu samples formed a distinct branch, whereas P23A/N2C/D282C clustered with WT. This consistent pattern across datasets demonstrates that rhodopsin misfolding produces a characteristic metabolic shift that is partially reversed upon structural correction.

3.4 | Heatmap Analysis Reveals Metabolic Suppression in P23A Cells and Partial Rescue in P23A/N2C/D282C

The heatmap provides a visualization of the relative metabolite abundances, with each colored cell representing the normalized intensity of a given metabolite (columns) across samples (rows) (Figure 4A). The heatmap of the top 50 significantly altered metabolites ($p < 0.05$) showed clear group-wise clustering aligned with rhodopsin folding status (Figure 4A). P23A TAC/NaBu cells displayed predominantly blue color intensities across many metabolites, indicating lower relative abundance compared to WT and P23A/N2C/D282C. In contrast, WT TAC/NaBu showed mixed but higher relative metabolite abundance, forming a distinct cluster consistent with a stable metabolic state. P23A/N2C/D282C TAC/NaBu cells exhibited an intermediate pattern shifting away from P23A and toward WT, demonstrating partial metabolic restoration following structural correction. WT and P23A N2C/D282C untreated cells clustered together, reflecting similar baseline metabolic profiles. Tight clustering of replicates confirmed dataset robustness and highlighted that rhodopsin misfolding drives broad metabolic suppression. Notably, this suppression was consistently observed across metabolites involved in glutathione metabolism, amino acid metabolism, and TCA cycle–associated intermediates, including L-glutamic acid, pyroglutamic acid, and fumaric acid. These patterns indicate that the heatmap structure is primarily shaped by coordinated changes in redox and mitochondrial pathways.

3.5 | Metabolites Differences in P23A and P23A/N2C/D282C

Pairwise reproducibility analysis of untreated versus TAC/NaBu-treated cells (Table 2) showed that both P23A and P23A/N2C/D282C rhodopsin-expressing cell lines share a stable core set of metabolites detected across independent experiments, confirming reproducible metabolic patterns upon rhodopsin expression. Across E1 and E2, P23A cells showed 80 consistent metabolites, while P23A/N2C/D282C exhibited 92 reproducible metabolites. The number of detected metabolites varied more across all experiments (Table S2) in P23A (119, 82, and 40), whereas P23A/N2C/D282C remained more stable (119 and 96), suggesting that the corrected mutant maintains a more consistent metabolic profile than the misfolded P23A.

Unique metabolites further distinguished the misfolded P23A from P23A/N2C/D282C. Seven metabolites, L-arginine,

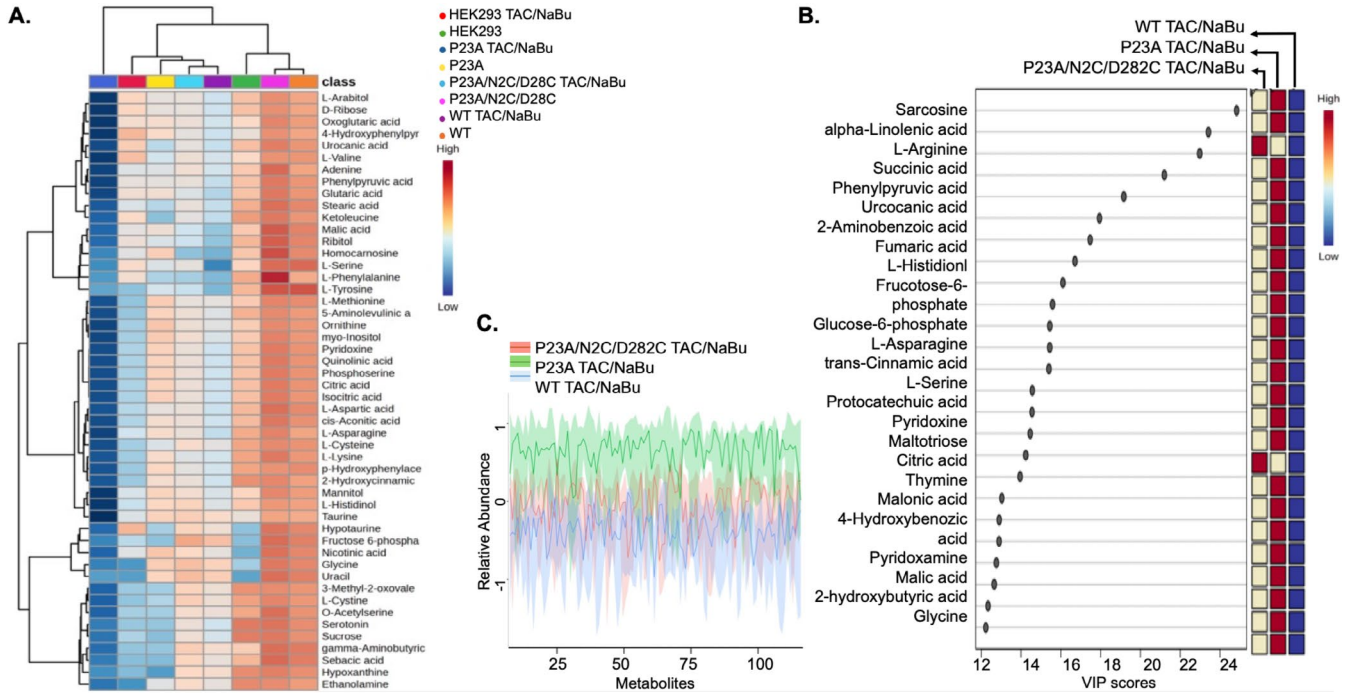

FIGURE 4 | Multivariate analysis of metabolomic features associated with rhodopsin folding status. (A) Heatmap of the top 50 significantly altered metabolites ($p < 0.05$), showing relative abundance patterns across WT, P23A, and P23A/N2C/D282C samples. (B) Variable Importance in Projection (VIP) plot from PLS-DA analysis showing the top 25 metabolites contributing to variance between groups (VIP > 1.2). (C) *K*-means clustering grouping samples into three clusters corresponding to WT, P23A, and P23A/N2C/D282C TAC/NaBu-treated conditions. These analyses identify key metabolites and patterns associated with rhodopsin misfolding and partial metabolic restoration upon structural correction.

L-leucine, mannitol, oleic acid, p-hydroxyphenylacetic acid, spermine, and trehalose, were uniquely enriched in P23A TAC/NaBu treated cells. Twenty-one metabolites were unique to P23A/N2C/D282C TAC/NaBu treated cells, including 2-hydroxycinnamic acid, cyclic AMP, D-mannose, fructose-6-phosphate, L-glutamine, myo-inositol, quinolinic acid, ribitol, serotonin, succinic acid, and palmitic acid. With WT cells, 105 metabolites were detected compared to P23A/N2C/D282C, which had 96 significant metabolites. WT cells showed three unique metabolites: L-cystine, L-valine, and stearic acid.

3.6 | VIP Analysis Identifies Key Discriminating Metabolites

PLS-DA and associated VIP scores were used to identify metabolites driving separation between WT, P23A, and P23A/N2C/D282C groups. VIP analysis highlighted the metabolites most responsible for distinguishing WT TAC/NaBu, P23A TAC/NaBu, and P23A/N2C/D282C TAC/NaBu groups. The VIP plot shown (Figure 4B) displays the top 25 metabolites (VIP > 1.2). Metabolites with the highest VIP scores have larger coefficients, such as sarcosine, alpha-linolenic acid, L-arginine, succinic acid, phenylpyruvic acid, and urocanic acid and they exert the strongest influence on sample separation. The accompanying color patterns illustrate the relative abundance of each metabolite across the three rhodopsin-expressing cell types, with red indicating higher levels and blue indicating lower levels. P23A TAC/NaBu samples show a consistent red-shift for many high-VIP metabolites, reflecting levels associated with misfolded rhodopsin. In contrast, WT TAC/NaBu samples displayed predominantly blue patterns, indicating lower and more tightly regulated metabolite abundance. The corrected mutant, P23A/N2C/D282C, exhibited intermediate colors, demonstrating partial restoration toward WT metabolic status. These VIP patterns indicate that a defined subset of metabolites, including L-arginine, succinic acid, phenylpyruvic acid, and urocanic acid, disproportionately contribute to the observed group differences. These pattern highlights a distinct biochemical signature associated with rhodopsin misfolding and show that structural rescue shifts key metabolites toward a more normalized and near restored profile.

3.7 | *K*-Means Clustering Identifies Three Metabolic States Aligned With Rhodopsin Folding Status

K-means clustering segregated the metabolomic data into three distinct unitless clusters corresponding to the metabolic states of the TAC/NaBu-treated rhodopsin cell lines (Figure 4C). Cluster 1 (red) contained the P23A/N2C/D282C TAC/NaBu, Cluster 2 (green) represented the P23A TAC/NaBu, and Cluster 3 (blue) comprised the WT TAC/NaBu. The clusters represent relative deviations from the mean. The mean metabolite profiles for each cluster revealed clear differences in overall abundance. Cluster 2 (P23A) showed the largest deviations from the mean across many metabolites, reflecting a broad metabolic shift associated with misfolded rhodopsin. In contrast, Cluster 3 (WT) displayed values closer to zero, indicating a more stable and tightly regulated metabolic pattern. Cluster 1 (P23A/N2C/D282C) showed intermediate deviations, consistent with partial restoration of

TABLE 2 | Pairwise reproducibility of biological replicates of common metabolites between P23A and P23A/N2C/D282C in experiments E1 and E2.

P23A: Untreated vs. Tac/NaBu (Total: 80)			P23A/N2C/D282C: Untreated vs. Tac/NaBu (Total: 92)		
2-Aminobenzoic acid	L-Arginine	Phosphoserine	2-Aminobenzoic acid	Guanosine	myo-Inositol
2-Hydroxybutyric acid	L-Asparagine	Protocatechuic acid	2-Hydroxybutyric acid	Homocarnosine	N-Acetylputrescine
3-Methyl-2-oxovaleric acid	L-Aspartic acid	Pyridoxamine	2-Hydroxycinnamic acid	Hypotaurine	O-Acetylserine
4-Hydroxyphenylpyruvic acid	L-Cystathionine	Pyridoxine	4-Hydroxybenzoic acid	Hypoxanthine	Ornithine
4-Hydroxyproline	L-Cysteine	Pyroglutamic acid	4-Hydroxyproline	Indoleacetic acid	Oxalic acid
Adenine	L-Histidine	Sarcosine	5-Aminolevulinic acid	Inosine	Oxoglutaric acid
Adenosine	L-Homoserine	Sebacic acid	Adenine	Isocitric acid	Palmitic acid
alpha-Hydroxyisobutyric acid	L-Isoleucine	Shikimic acid	Adenosine	Ketoleucine	Phenylpyruvic acid
alpha-Tocopherol	L-Leucine	Spermidine	alpha-Hydroxyisobutyric acid	L-Alanine	Phosphoserine
Aminocaproic acid	L-Lysine	Spermine	alpha-Linolenic acid	L-Asparagine	Protocatechuic acid
beta-Alanine	L-Methionine	Sucrose	Aminocaproic acid	L-Aspartic acid	Putrescine
cis-Aconitic acid	L-Norleucine	Taurine	beta-Alanine	L-Cystathionine	Pyridoxamine
Citric acid	L-Phenylalanine	Thymine	cis-Aconitic acid	L-Cysteine	Pyridoxine
Cysteamine	L-Proline	trans-Cinnamic acid	Citric acid	L-Glutamine	Pyroglutamic acid
D-Ribose 5-phosphate	L-Serine	Trehalose	Cyclic AMP	L-Histidine	Quinolinic acid
Deoxyadenosine	L-Threonine	Uracil	Cysteamine	L-Histidinol	Ribitol
Ethanolamine	L-Tyrosine	Uridine	D-Mannose	L-Homoserine	Sarcosine
Ferulic acid	Linoleic acid	Uridine diphosphate-N-acetylglucosamine	D-Ribose	L-Isoleucine	Sebacic acid
Fumaric acid	Malic acid		D-Ribose 5-phosphate	L-Lysine	Serotonin
gamma-Aminobutyric acid	Malonic acid		Deoxyadenosine	L-Methionine	Shikimic acid
Glutaric acid	Mannitol		Ethanolamine	L-Norleucine	Spermidine
Glutathione	Methylmalonic acid		Ferulic acid	L-Phenylalanine	Succinic acid
Glycerol	N-Acetylputrescine		Fructose 6-phosphate	L-Proline	Sucrose
Glycine	Niacinamide		Fumaric acid	L-Serine	Taurine
Glycolic acid	Nicotinic acid		gamma-Aminobutyric acid	L-Threonine	Thymine
Guanosine	O-Acetylserine		Glucose 6-phosphate	L-Tryptophan	trans-Cinnamic acid

(Continues)

TABLE 2 | (Continued)

P23A: Untreated vs. Tac/NaBu (Total: 80)		P23A/N2C/D282C: Untreated vs. Tac/NaBu (Total: 92)		
Homocarnosine	Oleic acid	Glutaric acid	L-Tyrosine	Uracil
Hypoxanthine	Ornithine	Glutathione	Linoleic acid	Uridine
Indoleacetic acid	Oxoglutaric acid	Glycerol	Malic acid	Uridine diphosphate-N-acetylglucosamine
Inosine	p-Hydroxyphenylacetic acid	Glycine	Malonic acid	Urocanic acid
L-Alanine	Phenylpyruvic acid	Glycolic acid	Methylmalonic acid	

metabolic balance following structural correction. These patterns align with the PCA and VIP results, confirming that rhodopsin misfolding drives a distinct metabolic phenotype that is partially reversed when the folding defect is corrected.

3.8 | Misfolded Rhodopsin Shows Six Metabolites Uniquely Associated With TAC/NaBu Treatment

To isolate metabolic changes specifically attributed to P23A, all metabolites that appeared in any HEK293 control treatment conditions were first removed to eliminate background cell-line effects (Table 3). Metabolites detected in untreated P23A cells were then removed from all treatment groups (TAC-only, NaBu-only, and TAC/NaBu treated). Finally, metabolites shared between TAC/NaBu-treated samples and either TAC-only or NaBu-only conditions were eliminated to exclude changes caused by individual reagents. After applying these filters, six metabolites remained uniquely associated with the P23A TAC/NaBu treated state: adenosine, L-allothreonine, L-cystine, malonic acid, protocatechuic acid, and 4-hydroxyproline.

3.9 | Differential Metabolite Signatures in TAC/NaBu Treated WT, P23A, and P23A/N2C/D282C

To characterize metabolic profiles associated with WT, P23A, and P23A/N2C/D282C, we performed pairwise differential metabolite analyses between TAC/NaBu-treated WT, P23A, and P23A/N2C/D282C (Figure 5). A fold change threshold of ≥ 1.0 was used only for exploratory visualization in volcano plots. Statistical significance was determined independently based on raw $p < 0.05$ and FDR adjusted $p < 0.1$.

Comparison of WT and P23A revealed widespread metabolic downregulation in cells expressing misfolded rhodopsin relative to WT. A volcano plot (Figure 5, Panel I-A) identified 99 significantly downregulated metabolites, with almost no increases, indicating a global suppression of metabolic activity. FDR-ranked significance (Panel I-B) highlighted prominent downregulation of metabolites such as L-asparagine, L-cysteine, hypotaurine, and glucose 6-phosphate. After eliminating untreated-baseline and single-treatment metabolites, a consistent subset remained specifically altered in P23A, including 2-aminobenzoic acid, 4-hydroxybenzoic acid, 4-hydroxyproline, alpha-lactose, cysteamine, L-cystine, L-glutamic acid, oxoglutaric acid, taurine, and urocanic acid (Table 4). Supplementary box plots (Figure S4) further confirmed these differences. Together, these results show that misfolded P23A rhodopsin induces strong metabolic repression.

P23A/N2C/D282C resulted in a metabolic profile distinct from the misfolded P23A background. Volcano plot (Figure 5, Panel II-A) revealed 68 significant metabolites, predominantly upregulated in P23A/N2C/D282C, consistent with restored metabolic capacity. Panel II-B included O-acetylserine, trehalose, and hypotaurine, all elevated in the structurally corrected rhodopsin. Across replicates, metabolites such as N-acetylputrescine, L-arginine, malic acid, and aminocaproic acid remained consistently lower in P23A than in P23A/N2C/D282C. After removing treatment- and background-derived metabolites, a refined set

TABLE 3 | Metabolites uniquely associated with misfolded rhodopsin (P23A).

HEK 293 untreated vs. Tac/NaBu	HEK 293 untreated vs. Tac			P23A untreated vs. Tac/NaBu		P23A untreated vs. Tac		P23A untreated vs. NaBu	Misfolded rhodopsin effect
beta-Alanine	1-Methylhistamine	Glutaric acid	myo-Inositol	1,3-Diaminopropane	L-Homoserine	2-Hydroxybutyric acid	L-Allothreonine	Adenine	Adenosine
D-Ribose 5-phosphate	2-Hydroxycinnamic acid	Histamine	Ornithine	3-Methyl-2-oxovaleric acid	L-Leucine	3-Methyl-2-oxovaleric acid	L-Glutamine	L-Histidinol	L-Allothreonine
Ethanolamine	3-Methyladenine	Histamine	Oxoglutaric acid	4-Hydroxyphenylpyruvic acid	L-Methionine	4-Hydroxyphenylpyruvic acid	L-Histidinol	L-Methionine	4-Hydroxyproline
Glucose 6-phosphate	4-Hydroxyphenylpyruvic acid	Hypotaurine	p-Hydroxyphenylacetic acid	Ethanolamine	L-Phenylalanine	Adenosine	L-Homoserine	Pyridoxamine	L-Cystine
Guanosine	Adenine	Ibuprofen	Phenylephrine	gamma-Aminobutyric acid	L-Serine	alpha-Tocopherol	L-Methionine	Tyramine	Malonic acid
Hypoxanthine	alpha-Linolenic acid	Isocitric acid	Phenylpyruvic acid	Glycine	Nicotinic acid	Deoxyadenosine	L-Phenylalanine		Protocatechuic acid
L-Homoserine	alpha-Tocopherol	L-Alanine	Phosphoserine	Hypotaurine	O-Acetylserine	Dihydrouracil	L-Valine		
L-Isoleucine	beta-Alanine	L-Arabitol	Pyridoxamine	Ketoleucine	Protocatechuic acid	Ethanolamine	O-Acetylserine		
L-Norleucine	cis-Aconitic acid	L-Asparagine	Pyridoxine	L-Histidine	Pyridoxamine	Glycine	Oleic acid		
L-Phenylalanine	Citric acid	L-Aspartic acid	Quinolinic acid	L-Histidinol	Sebacic acid	Guanosine	Palmitic acid		
O-Acetylserine	D-Mannose	L-Cysteine	Ribitol		Tyramine	Histamine	Pyridoxamine		
Pyridoxamine	D-Ribose	L-Histidine	Stearic acid		Uridine diphosphate-N-acetylglucosamine	Ketoleucine	Sarcosine		
Sebacic acid	D-Ribose 5-phosphate	L-Lysine	Succinic acid				trans-Cinnamic acid		
Uridine diphosphate-N-acetylglucosamine	Diaminopimelic acid	L-Methionine	trans-Cinnamic acid				Tyramine		
	Fructose 6-phosphate	L-Proline	Tyramine				Uridine diphosphate-N-acetylglucosamine		
	Glucose 6-phosphate	L-Threonine	Uracil						
		L-Tyrosine	Uridine						
		L-Valine	Uridine diphosphate-N-acetylglucosamine						
		Linoleic acid							
		Malic acid							
		Mannitol							

HEK 293 untreated vs. NaBu	HEK 293 Tac/NaBu vs. Tac				HEK 293 Tac/NaBu vs. NaBu	P23A Tac/NaBu vs. NaBu	P23A Tac/NaBu vs. Tac
1,3-Diaminopropane	1-Methylhistamine	D-Ribose	L-Asparagine	p-Hydroxyphenylacetic acid	Hydroxyphenylpyruvic acid	Adenine	2-Hydroxybutyric acid
3-Methyl-2-oxovaleric acid	2-Hydroxycinnamic acid	Diaminopimelic acid	L-Aspartic acid	Phenylpyruvic acid	D-Ribose	Ethanolamine	4-Hydroxyproline
4-Hydroxyphenylpyruvic acid	3-Methyl-2-oxovaleric acid	Ethanolamine	L-Glutamine	Phosphoserine	D-Ribose 5-phosphate	Glycine	alpha-Linolenic acid
Deoxyadenosine	3-Methyladenine	Fructose 6-phosphate	L-Histidinol	Pyridoxamine	Ethanolamine	Hypotaurine	alpha-Tocopherol
Ethanolamine	3,4-Dihydroxybenzeneacetic acid	gamma-Aminobutyric acid	L-Homoserine	Ribitol	Fructose 6-phosphate	L-Cysteine	Dihydrouracil
Fructose 6-phosphate	4-Hydroxyphenylpyruvic acid	Glutathione	L-Isoleucine	Serotonin	Guanosine	L-Cystine	Ethanolamine
gamma-Aminobutyric acid	5-Aminolevulinic acid	Guanosine	L-Leucine	Stearic acid	Ketoleucine	O-Acetylserine	Glycine
Hypoxanthine	alpha-Linolenic acid	Histamine	L-Lysine	Sucrose	L-Norleucine	Sebacic acid	Histamine
Ketoleucine	beta-Alanine	Homocarnosine	L-Methionine	Trehalose			Hypotaurine
Palmitic acid	cis-Aconitic acid	Hypoxanthine	L-Norleucine	Tyramine			L-Norleucine
Phenylephrine	Citric acid	Ibuprofen	L-Proline	Uridine diphosphate-N-acetylglucosamine			L-Serine
Putrescine	D-Mannose	Inosine	L-Serine				Malonic acid
Pyridoxamine		Isocitric acid	L-Tryptophan				Oleic acid
Sebacic acid		L-Arabitol	L-Tyrosine				Sarcosine
Spermine			Malic acid				Sebacic acid
Uridine diphosphate-N-acetylglucosamine			Mannitol				
			myo-Inositol				
			O-Acetylserine				
			Ornithine				

Note: To identify metabolites uniquely induced by the combined Tac/NaBu treatment, we eliminated all metabolites present in untreated cells compared with any treatment condition (Tac/NaBu, Tac alone, or NaBu alone). We further removed all metabolites shared between Tac/NaBu and the individual treatments (Tac-only or NaBu-only). After subtracting untreated-baseline metabolites and single-treatment overlaps, the remaining metabolites represent those specific to the P23A Tac/NaBu treatment.

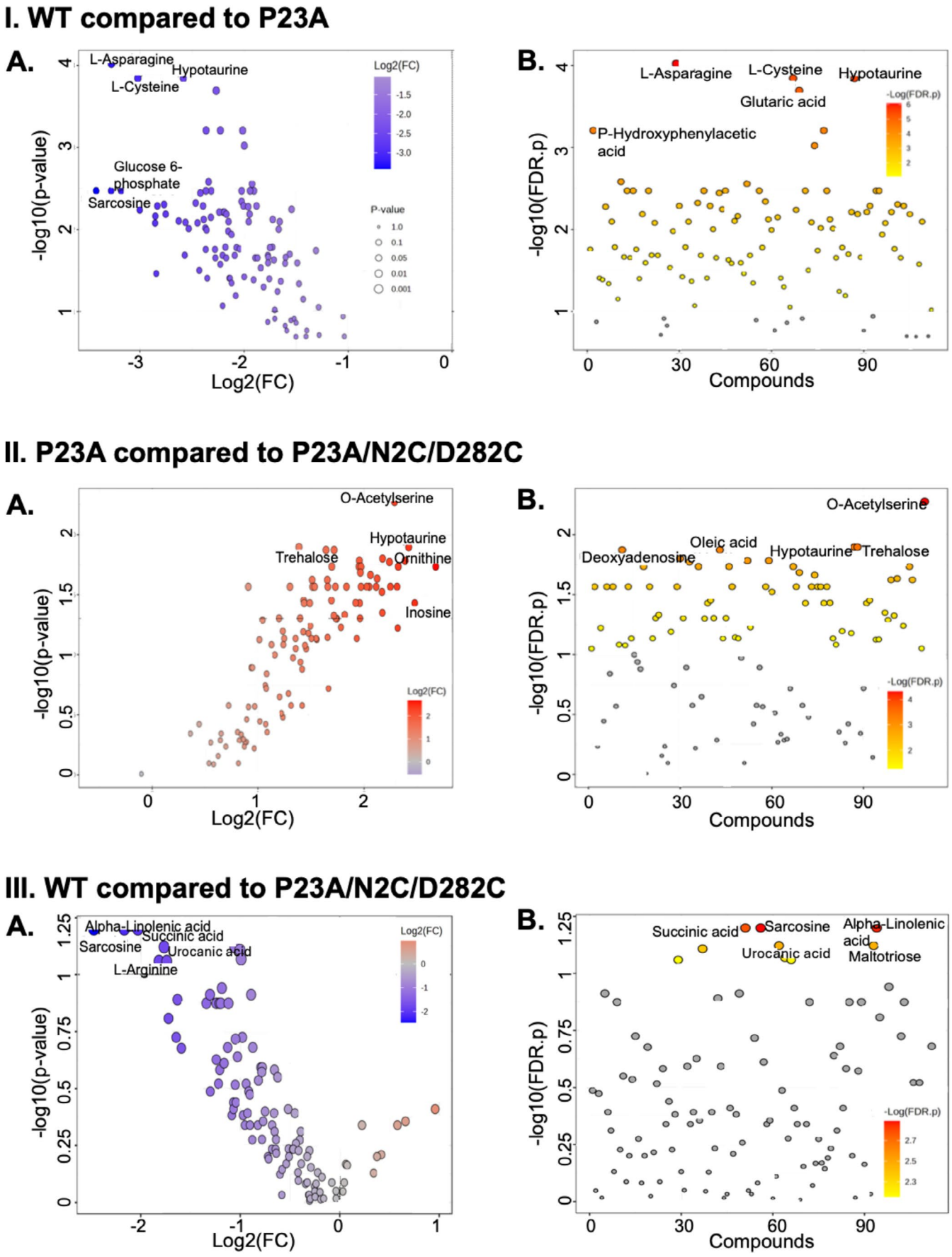

FIGURE 5 | Legend on next page.

FIGURE 5 | Differential metabolite analysis across rhodopsin conditions. Pairwise comparisons of TAC/NaBu-treated WT, P23A, and P23A/N2C/D282C samples. For each comparison: (A) Volcano plots showing fold change versus statistical significance (raw $p < 0.05$). (B) Scatter plots showing FDR-ranked metabolite significance. (I) WT vs. P23A: Widespread downregulation of metabolites in P23A. (II) P23A vs. P23A/N2C/D282C: Increased metabolite levels in corrected cells. (III) P23A/N2C/D282C vs. WT: Limited differences relative to WT. These results demonstrate global metabolic suppression in P23A and partial recovery following structural correction.

TABLE 4 | Rhodopsin metabolites effect in pairwise comparison of Tac/NaBu treated WT, P23A, and P23A/N2C/D28 after baseline effect elimination.

WT vs. P23A (Tac/NaBu)	WT vs. P23A/N2C/D282C (Tac/NaBu)	P23A vs. P23A/N2C/D282C (Tac/NaBu)	
2-Aminobenzoic acid	4-Hydroxybenzoic acid	Adenosine	4-Hydroxyproline
4-Hydroxybenzoic acid	Fumaric acid	L-Cystathionine	alpha-Hydroxyisobutyric acid
4-Hydroxyproline	L-Arginine	Methylmalonic acid	Aminocaproic acid
Alpha-Lactose	L-Cystine	Protocatechuic acid	Cyclic AMP
Cysteamine	Malonic acid	Pyroglutamic acid	Glycolic acid
L-Cystine	Protocatechuic acid	Tryptamine	Indoleacetic acid
L-Glutamic acid	Thymine	L-Glutamic acid	N-Acetylputrescine
Oxoglutaric acid	Urocanic acid		Spermidine
Taurine			
Urocanic acid			

of metabolites associated with P23A/N2C/D282C structural correction emerged, including L-cystathionine, methylmalonic acid, protocatechuic acid, pyroglutamic acid, tryptamine, L-glutamic acid, 4-hydroxyproline, alpha-hydroxyisobutyric acid, aminocaproic acid, cyclic AMP, glycolic acid, indoleacetic acid, N-acetylputrescine, and spermidine, which shift toward a partial restoration state in the P23A/N2C/D282C.

Comparison of the WT with P23A/N2C/D282C revealed 9 significantly downregulated metabolites relative to WT (Figure 5, Panels III-A,B). Downregulated metabolites in the P23A/N2C/D282C included ornithine, UDP, L-lysine, palmitic acid, guanosine, uracil, D-ribose, 5-aminolevulinic acid, L-methionine, hypoxanthine, and sucrose. After removing reagent and HEK293 background effects, a refined list of distinguishing metabolites included 4-hydroxybenzoic acid, fumaric acid, L-arginine, L-cystine, malonic acid, protocatechuic acid, thymine, and urocanic acid (Table 4). Shared metabolites across comparisons such as protocatechuic acid, L-cystine, and urocanic acid suggest a core metabolic signature of rhodopsin misfolding and its correction. The full list of statistically significant metabolites, along with box plots for all comparisons, is presented in Table S3 and Figure S1.

3.10 | Significant Metabolic Pathways Associated With Rhodopsin Misfolding and Structural Correction

Pathway enrichment of the final metabolite set derived from pairwise comparison (Table 5) revealed that rhodopsin misfolding in P23A cells disrupts several core metabolic pathways, many of which are partially restored in the structurally corrected P23A/N2C/D282C cells. The most significantly affected pathways (Figure 6A) were arginine biosynthesis ($p = 3.0 \times 10^{-5}$) and arginine and proline metabolism ($p = 1.1 \times 10^{-5}$) with associated metabolites including L-arginine, 4-hydroxyproline, fumaric acid, L-glutamic acid, and N-acetylputrescine. Taurine and hypotaurine metabolism (taurine and cysteamine), glutathione metabolism (pyroglutamic acid, L-glutamic acid, and spermidine), and alanine/aspartate/glutamate metabolism were also significantly impacted ($p < 0.01$), consistent with redox imbalance and mitochondrial stress associated with the misfolded P23A protein [54, 55].

MSEA analysis further highlighted histidine metabolism, cysteine and methionine metabolism, and butanoate metabolism as key pathways altered across genotypes (Figure 6B). To visualize these changes within broader biochemical networks, all significantly altered metabolites were integrated into a KEGG-based metabolic map (Figure 6C). Together, these results demonstrate that rhodopsin misfolding produces a characteristic metabolic signature dominated by amino-acid and redox pathways. Among these, arginine/proline metabolism, glutathione metabolism, and taurine/hypotaurine metabolism emerged as the most consistently altered and central pathways across analyses, suggesting that they represent primary metabolic nodes associated with misfolding. In contrast, other pathways identified through enrichment analysis likely reflect secondary or downstream responses to cellular stress. Full metabolite-level statistics, pathway significance values are provided in Table S4. Across analyses, the convergence of multivariate, differential, and pathway-level results highlights a core metabolic signature centered on amino acid metabolism, redox balance, and mitochondrial intermediates as the primary drivers of the observed phenotype.

4 | Discussion

To our knowledge, this study presents the first untargeted GC–MS–based metabolomic analysis linking rhodopsin misfolding

TABLE 5 | Final metabolites list from pairwise comparison of Tac/NaBu treated WT, P23A, and P23A/N2C/D28 and associated pathways.

Metabolites	Sig* pathways ($p < 0.05$)	Pairwise comparison
2-Aminobenzoic acid	Tryptophan metabolism*	WT vs. P23A
4-Hydroxybenzoic acid	Ubiquinone and other terpenoid-quinone biosynthesis	WT vs. P23A; WT vs. P23A/N2C/D282C
4-Hydroxyproline	Arginine and proline metabolism*	WT vs. P23A; P23A vs. P23A/N2C/D282C
Adenosine	Purine metabolism	P23A vs. P23A/N2C/D282C
alpha-Hydroxyisobutyric acid	Fatty acid degradation	P23A vs. P23A/N2C/D282C
Alpha-Lactose	Galactose metabolism	WT vs. P23A
Aminocaproic acid	Lysine metabolism	P23A vs. P23A/N2C/D282C
Cyclic AMP	cAMP signaling, Purine Metabolism	P23A vs. P23A/N2C/D282C
Cysteamine	Taurine and hypotaurine metabolism*, Methionine metabolism	WT vs. P23A
Fumaric acid	Arginine biosynthesis*, Alanine, aspartate and glutamate metabolism*, Pyruvate metabolism, Tyrosine metabolism	WT vs. P23A/N2C/D282C
Glycolic acid	Glyoxylate and dicarboxylate metabolism	P23A vs. P23A/N2C/D282C
Indoleacetic acid	Tryptophan metabolism*	P23A vs. P23A/N2C/D282C
L-Arginine	Arginine biosynthesis*, Arginine and proline metabolism*, Urea cycle	WT vs. P23A/N2C/D282C
L-Cystathionine	Cysteine and methionine metabolism, Glycine, serine and threonine metabolism, Suflur amino acid metabolism	P23A vs. P23A/N2C/D282C
L-Cystine	Cysteine and methionine metabolism, Suflur amino acid metabolism	WT vs. P23A; WT vs. P23A/N2C/D282C
L-Glutamic acid	Arginine biosynthesis*, Arginine and proline metabolism*, Glutathione metabolism*, Alanine, aspartate and glutamate metabolism*, Butanoate metabolism*, Histidine metabolism*, Citrate cycle (TCA cycle)*, Nitrogen Metabolism, Porphyrin metabolism	WT vs. P23A; WT vs. P23A/N2C/D282C; P23A vs. P23A/N2C/D282C
Malonic acid	Fatty acid biosynthesis	WT vs. P23A/N2C/D282C
Methylmalonic acid	Valine, leucine and isoleucine degradation, Vitamin B12 metabolism	P23A vs. P23A/N2C/D282C
N-Acetylputrescine	Arginine and proline metabolism*, Polyamine biosynthesis	P23A vs. P23A/N2C/D282C
Protocatechuic acid	Benzoate metabolism	WT vs. P23A/N2C/D282C P23A vs. P23A/N2C/D282C
Pyroglutamic acid	Glutathione metabolism*	P23A vs. P23A/N2C/D282C
Spermidine	Arginine and proline metabolism*, Glutathione metabolism*, beta-Alanine metabolism	P23A vs. P23A/N2C/D282C
Taurine	Taurine and hypotaurine metabolism*	WT vs. P23A
Thymine	Pyrimidine metabolism	WT vs. P23A/N2C/D282C
Tryptamine	Tryptophan metabolism*	P23A vs. P23A/N2C/D282C
Urocanic acid	Histidine metabolism*	WT vs. P23A; WT vs. P23A/N2C/D282C

to global metabolic remodeling in a controlled inducible cell system. We demonstrate that expression of misfolded P23A rhodopsin induces widespread and reproducible metabolic reprogramming, particularly affecting amino acid metabolism, redox homeostasis, nucleotide turnover, and mitochondrial intermediates. Structural correction through the N2C/D282C

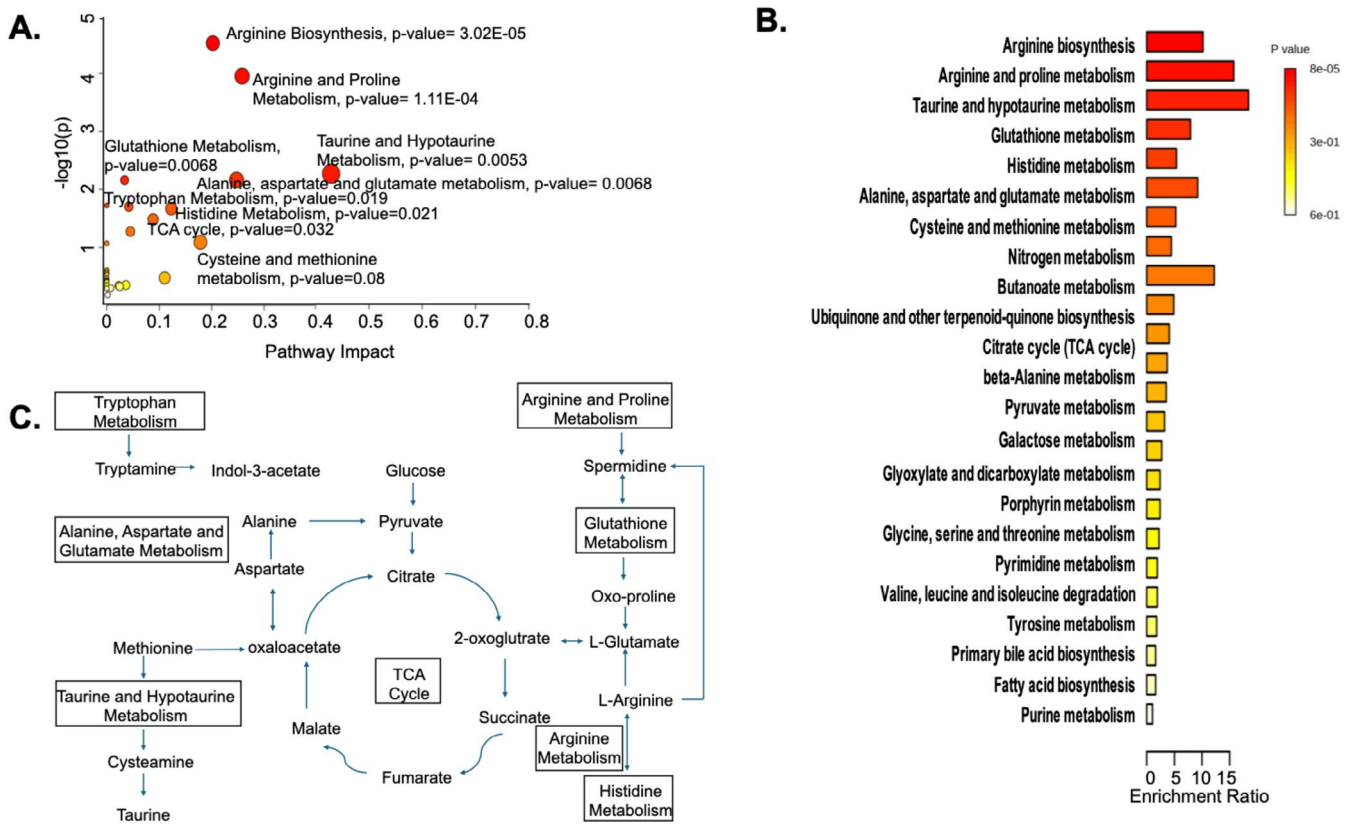

FIGURE 6 | Metabolic pathway enrichment reveals key perturbations in misfolded rhodopsin-expressing cells. (A) Pathway impact analysis using MetaboAnalyst highlights the most significantly dysregulated metabolic pathways in P23A compared to WT and P23A/N2C/D282C. (B) MSEA bar plot shows the top enriched pathways based on enrichment ratio and *p*-value. The color gradient from yellow to red denotes increasing statistical significance (lower *p*-values). (C) KEGG Pathway Mapping of Differential Metabolites.

disulfide bond partially restores these metabolic perturbations, establishing a direct biochemical link between rhodopsin folding integrity and cellular metabolic state. As this study employs a non-retinal cellular model, these findings should be interpreted as conserved, intrinsic cellular responses to rhodopsin misfolding and proteostatic stress largely at the level of ER stress rather than a direct representation of retinal degeneration. Consistent with prior biochemical studies, structural correction of P23A results in near functional recovery [5], providing important context for the intermediate metabolic state observed here.

Pairwise analyses revealed that P23A exhibits global metabolic suppression, with downregulation of metabolites such as L-asparagine, L-cysteine, hypotaurine, and glucose-6-phosphate, consistent with impaired amino acid metabolism, redox imbalance, and glycolytic flux [56]. These findings align with prior reports linking rhodopsin misfolding to mitochondrial dysfunction and proteostatic stress [10, 57]. The observed depletion of redox-associated metabolites, including taurine, hypotaurine, glutathione intermediates, and L-cystine, further supports a state of oxidative stress and compromised antioxidant buffering [58–60]. Baseline filtering enabled identification of metabolites specifically associated with the misfolded P23A state, independent of treatment or HEK293 background effects. Metabolites such as adenosine, L-allothreonine, L-cystine, malonic acid, protocatechuic acid, and 4-hydroxyproline were uniquely retained in P23A cells, implicating disruptions in nucleotide metabolism, lipid remodeling, and antioxidant defense pathways [61–63]. Importantly, protocatechuic acid is a benzoate-derived metabolite with established antioxidant properties, and its selective retention likely reflects a compensatory antioxidant response to rhodopsin misfolding, consistent with prior reports linking oxidative stress to photoreceptor degeneration in rhodopsin-associated retinal diseases [64]. Malonic acid, in particular, has been associated with altered lipid metabolism and mitochondrial inhibition, processes critical for maintaining photoreceptor membrane integrity [65]. In contrast, WT cells retained metabolites such as L-cystine, L-valine, and stearic acid that were depleted or absent in the misfolded P23A, consistent with preserved amino acid balance, lipid metabolism, and redox homeostasis under properly folded rhodopsin expression [56, 61, 66, 67].

Comparisons between P23A and P23A/N2C/D282C highlighted amino acid metabolism as a central node of metabolic stress, including perturbations in L-glutamic acid, L-cystathionine, and arginine-related pathways. Arginine and proline metabolism emerged as the most significantly enriched pathways, consistent with reports linking altered arginine handling and urea-cycle intermediates to retinal degeneration [29, 54]. Proline metabolism is particularly relevant in retinal biology, as the RPE relies on proline as a major mitochondrial fuel, supplying glutamate, ornithine, and polyamines to photoreceptors [68, 69]. Notably, mutations in key proline metabolism genes, including ornithine aminotransferase (OAT), ALDH18A1, and PYCR1, are associated with inherited retinal degeneration, underscoring

the functional importance of this pathway for retinal and RPE metabolic support [68, 69]. Disruption of this metabolic axis may therefore directly compromise retinal support functions. Polyamine metabolism was also implicated through elevated spermidine and N-acetylputrescine, metabolites commonly associated with cellular stress, apoptosis, and autophagy [70]. These findings, together with dysregulated glutathione intermediates, indicate engagement of stress-response networks downstream of rhodopsin misfolding. Consistent with this interpretation, Sánchez-Vallejo et al. demonstrated that in rd1 and rd10 mouse models of RP, expression of glutamate cysteine ligase (GCLC), the rate-limiting enzyme in glutathione biosynthesis, is dynamically regulated during photoreceptor degeneration, with elevated expression during periods of heightened oxidative stress [60]. Similarly, in our misfolded P23A, we observed significant perturbations in glutathione-related metabolites, including L-cystine, L-cystathionine, L-arginine, L-glutamic acid, and pyroglutamic acid, reinforcing the hypothesis that impaired redox homeostasis is a hallmark of rhodopsin misfolding. Consistent perturbation of TCA-cycle intermediates, including fumaric acid, malonic acid, and oxoglutaric acid across multiple comparisons, supports impaired mitochondrial metabolism in P23A [58, 71]. These observations align with prior studies demonstrating compromised oxidative phosphorylation and energy failure in RP models expressing misfolded rhodopsin [10]. At the pathway level, taurine and hypotaurine metabolism emerged as significantly enriched, consistent with redox dysregulation [58]. Enrichment of glutathione metabolism together with alanine/aspartate/glutamate metabolism further supports oxidative stress–linked mitochondrial perturbation in the misfolded rhodopsin state [59, 60]. These coordinated perturbations suggest impaired metabolic flexibility rather than isolated pathway failure. In photoreceptors, bioenergetic homeostasis is maintained through specialized adaptations, including mini-Krebs cycles and Cori–Cahill cycle–like shuttles, which support redox balance and energy production under high metabolic demand [58]. Disruption of TCA intermediates together with taurine/hypotaurine and glutathione metabolism in P23A cells is therefore consistent with a loss of such metabolic adaptability, which is partially restored following structural correction.

Multivariate analyses (PCA, clustering, heatmaps, and PERMANOVA) consistently showed that P23A/N2C/D282C rhodopsin adopts an intermediate metabolic state, shifting toward but not fully overlapping with WT profiles. In contrast, TAC/NaBu-treated P23A cells formed a distinct metabolic cluster, clearly separating from both WT and P23A/N2C/D282C conditions, indicating that rhodopsin misfolding imposes a unique metabolic signature that is only partially reversed upon structural correction. The metabolic restoration observed in P23A/N2C/D282C cells is consistent with prior biochemical characterization showing that disulfide bond–mediated correction largely reverses the P23A folding defect and restores rhodopsin properties toward WT levels [5]. Similarly, our metabolomic analyses demonstrated near-complete reversal of the P23A-associated metabolic phenotype, supporting a strong coupling between rhodopsin folding integrity and cellular metabolism. Key discriminating metabolites contributing to this separation included L-arginine, L-glutamic acid, pyroglutamic acid, methylmalonic acid, and cyclic AMP, implicating disruptions in amino acid metabolism, redox homeostasis, and mitochondrial intermediates, consistent with prior reports of altered mitochondrial markers in P23H RP models [58, 71, 72]. PERMANOVA confirmed that misfolded P23A represents the most divergent metabolic state, while the corrected variant exhibits partial convergence toward WT, accounting for a substantial proportion of variance in the dataset. Notably, metabolites such as cyclic AMP and indoleacetic acid were uniquely detected in the corrected P23A/N2C/D282C cells, suggesting restoration of secondary messenger signaling and tryptophan-derived pathways. The presence of 4-hydroxybenzoic acid, a precursor in ubiquinone biosynthesis, and fumaric acid, a TCA-cycle intermediate, further supports improved mitochondrial function and energy metabolism [72]. After eliminating baseline treatment and HEK293 background effects, a refined set of discriminating metabolites included 4-hydroxybenzoic acid, fumaric acid, L-arginine, L-cystine, malonic acid, protocatechuic acid, thymine, and urocanic acid, spanning energy metabolism, redox balance, and amino acid/nucleotide turnover [29, 56, 61]. These findings parallel reports by Rowe et al., where supplementation with TCA-cycle intermediates enhanced photoreceptor survival in autosomal recessive RP models [72].

The metabolic reprogramming observed in P23A cells is consistent with early ER proteostatic stress driven by Class II rhodopsin mutations [3, 4]. Accumulation of misfolded rhodopsin in the ER activates UPR sensors such as IRE1, PERK, and ATF6, initiating transcriptional programs that modulate amino acid metabolism, redox homeostasis, and mitochondrial function [3, 64]. Altered glutathione metabolism, arginine/proline biosynthesis, and suppression of TCA intermediates observed here are consistent with downstream effects of UPR signaling mediated by transcription factors such as ATF4 and CHOP [64, 73]. In addition, several metabolite changes may reflect increased ER-associated degradation (ERAD) and recycling of misfolded rhodopsin [74]. Enhanced proteasomal degradation would be expected to elevate intracellular amino acid pools, nitrogen intermediates, and nucleotide turnover products, consistent with the detection of adenosine, L-cystine, L-glutamic acid, and polyamine intermediates in the misfolded P23A state [74]. Partial normalization of these pathways in the P23A/N2C/D282C supports a causal relationship between rhodopsin folding burden, UPR/ERAD engagement, and downstream metabolic remodeling. Together, these findings suggest that UPR-driven ERAD and sustained proteasomal recycling of misfolded rhodopsin contribute to the observed shifts in amino acid availability, redox buffering, and mitochondrial intermediates [75].

Previous metabolomics studies in RP, including analyses of rd10 mouse retinas and P23H-expressing cell models, have reported disruptions in nucleotide metabolism, fatty acid oxidation, oxidative stress, and mitochondrial function [10, 29]. However, these systems involve complex in vivo contexts or lack endogenous rhodopsin expression, complicating the interpretation of folding-specific effects. The inducible HEK293S-GnTI$^-$ system used here enables controlled rhodopsin expression independent of retinal chromophore metabolism, allowing direct interrogation of misfolding-driven metabolic consequences. Although rhodopsin is retina-specific, the cellular stress pathways engaged by its misfolding, including UPR activation, ERAD, oxidative stress, and metabolic reprogramming, are conserved across cell types [76]. Thus, while photoreceptors may be uniquely

vulnerable due to high metabolic demand, the core proteostasis metabolism coupling identified here likely reflects generalizable responses to chronic ER proteotoxic stress.

The specific metabolic axes we resolve here—glutathione-centered redox balance, arginine and proline metabolism, TCA anaplerosis, and mitochondrial dicarboxylate intermediates—are precisely the axes under highest physiological demand in photoreceptors. Photoreceptors exhibit the highest per-gram oxygen consumption of any tissue in the body [77, 78], maintain an unusually high glutathione: glutathione disulfide turnover to buffer continuous photo-oxidative load, and rely on the visual cycle, which is itself a major endogenous source of reactive aldehydes and oxidative byproducts. Du et al. [79] and the Hurley laboratory [80, 81] have shown that photoreceptors are aerobic-glycolytic but also depend heavily on glutamine- and aspartate-driven TCA anaplerosis to sustain biosynthetic demand for outer-segment renewal, with proline and serine acting as accessory substrates.

The implication is direct: every metabolic vulnerability we expose in HEK293S-GnTI$^-$ cells corresponds to a pathway already operating near capacity in photoreceptors. Misfolded-rhodopsin-driven glutathione consumption, NADPH drain, and anaplerotic load are therefore expected to be amplified, not attenuated, in the retinal context, where baseline reserve is lower and the consequences of redox failure include lipid peroxidation of outer-segment membranes and photoreceptor apoptosis. This convergence strengthens, rather than weakens, the translational relevance of the HEK293 model for identifying metabolic intervention nodes. This convergence does not erase the limitations of a non-retinal model, and we acknowledge that absolute pool sizes and flux magnitudes will differ between cell types.

4.1 | A Two-Node Framework for the Metabolic Phenotype of Misfolded Rhodopsin

The breadth of metabolic changes reported here is best understood not as a collection of parallel independent pathway perturbations, but as the coordinated downstream output of two tightly interlocked primary upstream nodes: PERK-arm activation of the UPR and a glutathione-centered redox imbalance. Misfolded P23A rhodopsin is retained in the ER and engages the UPR, with the PERK→eIF2α→ATF4 branch acting as the principal transcriptional driver of the metabolic phenotype [73]. The ATF4 program directly transactivates the amino acid transporters (SLC7A11, SLC1A4/5, SLC3A2), asparagine synthetase (ASNS), the serine–glycine biosynthetic enzymes (PHGDH, PSAT1, PSPH), the proline biosynthetic axis (ALDH18A1/P5CS, PYCR1/2), the mitochondrial one-carbon enzyme MTHFD2, and the glutathione rate-limiting enzyme GCLC [82, 83]. This single transcriptional node parsimoniously accounts for the rescue-sensitive shifts we observe in arginine, proline, hydroxyproline, glutamic acid, pyroglutamic acid, asparagine, glycine, serine, and cystine.

The second, mechanistically coupled node is the glutathione/redox axis. ATF4-driven GCLC induction is itself a redox response, and ongoing glutathione synthesis is a major sink for cysteine and glutamate while draining glycine, explaining their coordinated depletion. Pyroglutamic acid accumulation is the diagnostic signature of γ-glutamyl cycle backup under glutathione demand [84], and the cystine, cysteamine, hypotaurine, and taurine intermediates we detect are all stations on the transsulfuration-to-taurine flux upregulated when glutathione turnover is high. Sustained glutathione biosynthesis and reductive biosynthetic demand impose an NADPH burden that pulls flux through the oxidative pentose phosphate pathway and forces TCA anaplerosis, providing a unified explanation for the elevated fumarate, succinate, and α-ketoglutarate pools. These mitochondrial intermediate shifts are further amplified by the mitochondrial dysfunction that follows persistent PERK signaling [85, 86].

Nucleotide and lipid-headgroup changes (altered pyrimidine intermediates, ethanolamine, phosphoethanolamine) are best interpreted as secondary compensations downstream of altered one-carbon flux and NADPH availability rather than as independent primary lesions. This two-node framework—PERK–ATF4 driving the amino acid and one-carbon arm, and the glutathione–redox axis driving the sulfur and anaplerotic arm, with bidirectional coupling between them, is consistent with the integrative view of ER-stress metabolism recently synthesized by Almanza et al. [87] and is supported by the P23H interactome data of Kim et al. [57], which independently identified engagement of proteostasis and redox quality-control machinery in the same mutant class. The metabolomic signature reported here is the metabolic shadow of those proteomic engagements, and the partial reversal observed in the disulfide-stabilized N2C/D282C rescue mutant indicates that both nodes are downstream of the primary folding defect rather than constitutive features of the expression system. The metabolic changes observed are largely consistent with ER stress and activation of the UPR/IPR pathways, and in particular the PERK-eIF2alpha-ATF4 arm of UPR which is responsible for altering regulation of genes involved in amino acid metabolism, protection against oxidative stress and protein homeostasis [88]. Furthermore, activation of the PERK branch of the UPR in a rhodopsin P23H rat model of RP has been reported previously [86].

P23A and P23H are both class II rhodopsin folding mutants at the identical residue within the hydrophilic N-terminal cap and abolish the same conserved polar contact stabilizing the β-sheet of the intradiscal plug; the biophysical lesion is therefore mechanistically analogous, and both variants exhibit the canonical ER-retention and UPR-engagement phenotype previously characterized for class II rhodopsin mutants [3, 9]. Clinically and biochemically, P23A is the milder of the two, with a higher residual fraction of correctly folded protein and slower disease progression. This positions P23A as a sensitive rather than divergent model: the metabolic perturbations detectable here against a partially preserved folding background are expected to be amplified, not absent, in P23H. Three lines of independent evidence support this prediction. Kim et al. [57] showed that the P23H interactome is enriched for ER proteostasis, ubiquitin-proteasome, and redox quality-control machinery, precisely the upstream apparatus whose metabolic output we resolve here. Liu et al. [10] reported P23H-associated mitochondrial and OXPHOS deficits that align directly with the TCA-intermediate shifts (fumarate, succinate, α-ketoglutarate) which we observe in P23A. Yu et al. [18] documented elevated photoreceptor oxidative stress and

glutathione demand in P23H transgenic models, consistent with the glutathione-axis perturbation we resolve metabolically. A direct head-to-head metabolomic comparison between P23A and P23H, ideally in matched inducible HEK293S-GnTI^{-} lines and ultimately in patient-derived retinal organoids, is an important future direction.

While the present study focuses on rhodopsin misfolding, it is important to consider that some of the observed metabolic changes may reflect broader cellular responses to chronic proteotoxic stress rather than being exclusively rhodopsin-specific. Accumulation of misfolded proteins is known to activate conserved stress pathways, including UPR and ERAD [76], which can induce overlapping metabolic reprogramming across different systems. Therefore, although our experimental design isolates folding-dependent effects within a controlled framework, we cannot fully exclude the possibility that similar metabolic signatures may arise from expression of other misfolded or aggregation-prone proteins. Future studies incorporating unrelated misfolded protein controls will be essential to distinguish rhodopsin-specific metabolic alterations from generalized proteostasis-driven responses.

Although several metabolic pathways, including purine metabolism, pyrimidine metabolism, fatty acid biosynthesis and degradation, glyoxylate and dicarboxylate metabolism, and cysteine and methionine metabolism, did not reach statistical significance in global pathway enrichment analysis, individual metabolites within these pathways were consistently altered across multiple pairwise comparisons. For example, adenosine, thymine, and cyclic AMP implicate perturbations in purine and pyrimidine metabolism, consistent with prior reports linking altered nucleotide turnover to cellular and ER stress during photoreceptor degeneration [30]. These findings align with the broad-spectrum metabolomics study by Weiss et al., which reported significant disruption of purine and pyrimidine metabolism, energy metabolism, and nitrosative stress in rd10 mouse retinas [29]. Although their model focused on a Pde6b mutation, the convergence on altered nucleotide and CoA-related metabolites parallels our observations of adenosine, thymine, and fumarate changes in P23A, suggesting mutation-independent metabolic stress signatures in RP. Similarly, methylmalonic acid and malonic acid intermediates of fatty acid and mitochondrial energy metabolism were consistently perturbed, supporting localized mitochondrial dysfunction [58]. The detection of glycolic acid, indoleacetic acid, and protocatechuic acid, linked to glyoxylate and tryptophan metabolism, further indicates that discrete metabolic nodes within otherwise non-significant pathways may still play functionally important roles. Together, these observations underscore the importance of metabolite-level interpretation alongside pathway-level analysis and suggest that metabolic reprogramming may represent an early hallmark of rhodopsin misfolding, even in the absence of overt retinal degeneration.

To further refine mechanistic interpretation, not all statistically significant metabolic changes were considered equally informative. Metabolites and pathways were prioritized based on consistency across comparisons, magnitude of change, enrichment in significant pathways, known links to proteostasis and ER stress, and their reversibility upon structural correction. Using these criteria, perturbations in glutathione metabolism, amino acid metabolism (particularly arginine and proline), and TCA cycle intermediates emerged as the most robust and biologically relevant features of the misfolded P23A state. These pathways are well aligned with established downstream consequences of UPR activation [69, 70], including redox imbalance, altered amino acid utilization, and mitochondrial dysfunction, and therefore likely represent primary metabolic responses to rhodopsin misfolding. In contrast, changes observed in nucleotide metabolism, lipid-associated intermediates, and benzoate- or tryptophan-derived metabolites are more consistent with secondary or compensatory adaptations to sustained proteotoxic stress [56–58]. Such changes could arise from increased turnover, stress signaling, or adaptive remodeling rather than direct coupling to rhodopsin folding status [14, 30, 38].

Several limitations warrant consideration. The stable cell lines used in this study represent pools of cells with random insertions of the expression cassette such that we do not know the chromosomal position of the opsin gene. The advantage is that there are no biased positional effects of the insertions because these cell line ‘pools’ will have many random insertions and not just one with a potentially positional effect as would be for a clonal cell line. If we wanted to investigate positional effects, we would need to create a landing site where single insertions will integrate which could be an interesting future study.

Certain metabolites, such as α-hydroxyisobutyric acid, may arise from extraction-related artifacts associated with MTBE use [90]. Additionally, benzoate- or amide-derived compounds may reflect low-level laboratory contamination [91]. Batch-to-batch variability was most pronounced in P23A, likely reflecting increased metabolic instability associated with misfolded protein stress. Nevertheless, consistent clustering, PCA separation, and PERMANOVA validation across independent experiments indicate that the core metabolic trends are robust and biologically meaningful.

These findings underscore the importance of integrating pathway-level enrichment with targeted metabolite-level interpretation to capture biologically meaningful perturbations that may be overlooked by global analyses. Together, the identified metabolite changes define a metabolic fingerprint of cellular dysfunction associated with P23A rhodopsin misfolding and may provide a rationale for exploring therapeutic strategies aimed at mitigating RP-associated cellular stress. These results position metabolic remodeling as an early and integral consequence of rhodopsin misfolding rather than a secondary byproduct of photoreceptor degeneration. The convergence of amino acid imbalance, redox dysregulation, altered nucleotide turnover, and impaired mitochondrial intermediates suggests that proteostasis stress imposed by misfolded rhodopsin propagates through tightly coupled metabolic networks [76, 92]. Importantly, the partial normalization of these pathways following P23A/N2C/D282C structural correction indicates that metabolic dysfunction is not irreversible but dynamically linked to folding burden and ER stress. This coupling between protein quality control and cellular metabolism highlights metabolic pathways as sensitive readouts of folding stress and potential points of therapeutic

intervention [92]. Future studies integrating flux analysis, targeted redox measurements, and cell-type–specific and in vivo retinal models will be essential to define whether modulation of these metabolic nodes can enhance proteostasis capacity and improve photoreceptor function across genetically diverse forms of RP.

From a translational perspective, the present findings suggest that metabolic modulation may represent a rational strategy to complement existing approaches targeting rhodopsin folding and gene-level correction. Based on the prioritization of pathways identified in this study, the most appeared intervention nodes lie within UPR modulation, redox regulation, amino acid metabolism, and mitochondrial function. Consistent perturbation of glutathione-related metabolites supports the potential for antioxidant-based strategies to enhance redox buffering capacity under proteotoxic stress [70, 73]. Similarly, alterations in arginine and proline metabolism, together with polyamine intermediates, point to amino acid supplementation or metabolic rebalancing as testable approaches to support cellular homeostasis [53, 64]. Disruption of TCA cycle intermediates further suggests that targeted support of mitochondrial metabolism may help mitigate energy deficits associated with rhodopsin misfolding [66, 70]. Importantly, these strategies should be viewed as complementary to primary interventions targeting rhodopsin folding or proteostasis, rather than as standalone therapies. Given that many of the identified metabolic changes likely reflect both direct consequences of misfolded rhodopsin and secondary adaptive responses, future studies integrating metabolic modulation with proteostasis-targeting approaches will be necessary to determine whether combinatorial interventions can enhance photoreceptor resilience. These findings provide a framework for developing testable hypotheses linking specific metabolic nodes to functional outcomes in more physiologically relevant retinal models.

Building on this framework, four pharmacologically tractable intervention nodes deserve explicit prioritization. First, direct restoration of glutathione capacity: N-acetylcysteine (NAC) and γ-glutamylcysteine bypass the rate-limiting GCLC step, and Nrf2 activators such as sulforaphane and dimethyl fumarate (the latter FDA-approved as Tecfidera) coordinately upregulate the glutathione biosynthetic and antioxidant response element battery [93, 94]. Second, replenishment of the arginine–proline axis: L-arginine and L-citrulline support both urea-cycle-coupled and collagen-prolyl-hydroxylase-coupled proline pools and have established retinal safety profiles. Third, anaplerotic TCA support: cell-permeable dimethyl-α-ketoglutarate restores α-KG-dependent dioxygenase activity and mitochondrial NADH balance [95]. Fourth, integrated stress response modulation: ISRIB and small-molecule PERK inhibitors (GSK2606414, GSK2656157) attenuate pathological PERK–eIF2α–ATF4 output [96, 97] but must be used cautiously since part of the ATF4 program (GCLC, ASNS, serine biosynthesis) is protective and complete ISR shutdown risks unmasking the proteotoxic stress itself [98]. A combinatorial regimen pairing modest ISR dampening with redox and anaplerotic support is therefore likely to outperform any single-agent strategy.

5 | Conclusion

This study provides the first comprehensive metabolomic assessment of rhodopsin misfolding using a tightly controlled inducible HEK293S cell system. We demonstrate that expression of misfolded P23A rhodopsin induces widespread metabolic dysregulation, disrupting pathways essential for cellular homeostasis, including mitochondrial energy metabolism, antioxidant defense, and amino acid biosynthesis. Importantly, structural correction of rhodopsin through disulfide bond engineering P23A/N2C/D282C partially restores these metabolic perturbations, establishing a direct functional link between rhodopsin folding integrity and cellular metabolic state. Metabolites associated with arginine and proline metabolism, glutathione metabolism, and the cycle were prominently affected in the misfolded state, indicating suppression of bioenergetic and redox-supporting pathways as a hallmark of rhodopsin misfolding. The partial normalization of these pathways following structural rescue highlights their dynamic sensitivity to folding burden and identifies metabolic nodes that may be leveraged therapeutically. Collectively, these findings identify metabolic remodeling as a central and early consequence of rhodopsin misfolding in RP and suggest that targeted metabolic interventions such as amino acid supplementation, antioxidant support, or enhancement of mitochondrial metabolism may complement existing therapies for photoreceptor degeneration.

Author Contributions

Judith Klein-Seetharaman and Philip J. Reeves designed the research; Hannah Staggs-Sandy and Philip J. Reeves created mutant cell lines; Meghana Hosahalli Shivananda Murthy prepared and analyzed samples from mutant cell lines; Meghana Hosahalli Shivananda Murthy and Paniz Jasbi collected and analyzed metabolomics data; Meghana Hosahalli Shivananda Murthy and Judith Klein-Seetharaman wrote the paper; Paniz Jasbi and Philip J. Reeves edited the paper. All authors read and approved the manuscript.

Funding

The authors have nothing to report.

Conflicts of Interest

The authors declare no conflicts of interest.

Data Availability Statement

The datasets supporting the findings of this study are available from the corresponding author upon reasonable request.

References

1. S. P. Daiger, S. J. Bowne, and L. S. Sullivan, "Genes and Mutations Causing Autosomal Dominant Retinitis Pigmentosa," *Cold Spring Harbor Perspectives in Medicine* 5 (2015): a017129.

2. F. Zhen, T. Zou, T. Wang, Y. Zhou, S. Dong, and H. Zhang, "Rhodopsin-Associated Retinal Dystrophy: Disease Mechanisms and Therapeutic Strategies," *Frontiers in Neuroscience* 17 (2023): 1132179.

3. D. Athanasiou, M. Aquila, J. Bellingham, et al., "The Molecular and Cellular Basis of Rhodopsin Retinitis Pigmentosa Reveals Potential Strategies for Therapy," *Progress in Retinal and Eye Research* 62 (2018): 1–23.

4. S. Kaushal and H. G. Khorana, "Structure and Function in Rhodopsin. 7. Point Mutations Associated With Autosomal Dominant Retinitis Pigmentosa," *Biochemistry* 33 (1994): 6121–6128.

5. C. A. Opefi, K. South, C. A. Reynolds, S. O. Smith, and P. J. Reeves, "Retinitis Pigmentosa Mutants Provide Insight Into the Role of the N-Terminal Cap in Rhodopsin Folding, Structure, and Function," *Journal of Biological Chemistry* 288 (2013): 33912–33926.

6. P. J. Reeves, J.-M. Kim, and H. G. Khorana, "Structure and Function in Rhodopsin: A Tetracycline-Inducible System in Stable Mammalian Cell Lines for High-Level Expression of Opsin Mutants," *Proceedings of the National Academy of Sciences of the United States of America* 99 (2002): 13413–13418.

7. M. P. Krebs, D. C. Holden, P. Joshi, C. L. Clark, A. H. Lee, and S. Kaushal, "Molecular Mechanisms of Rhodopsin Retinitis Pigmentosa and the Efficacy of Pharmacological Rescue," *Journal of Molecular Biology* 395 (2010): 1063–1078.

8. S. M. Noorwez, V. Kuksa, Y. Imanishi, et al., "Pharmacological Chaperone-Mediated In Vivo Folding and Stabilization of the P23H-Opsin Mutant Associated With Autosomal Dominant Retinitis Pigmentosa," *Journal of Biological Chemistry* 278 (2003): 14442–14450.

9. J. Mitchell, F. Balem, K. Tirupula, et al., "Comparison of the Molecular Properties of Retinitis Pigmentosa P23H and N15S Amino Acid Replacements in Rhodopsin," *PLoS One* 14 (2019): e0214639.

10. Y. Liu, X. Wang, R. Gong, G. Xu, and M. Zhu, "Overexpression of Rhodopsin or Its Mutants Leads to Energy Metabolism Dysfunction in 661w Cells," *Investigative Ophthalmology & Visual Science* 63 (2022): 2.

11. R. V. S. Rajala, A. Rajala, C. Kooker, Y. Wang, and R. E. Anderson, "The Warburg Effect Mediator Pyruvate Kinase M2 Expression and Regulation in the Retina," *Scientific Reports* 6 (2016): 37727.

12. C. Punzo, W. Xiong, and C. L. Cepko, "Loss of Daylight Vision in Retinal Degeneration: Are Oxidative Stress and Metabolic Dysregulation to Blame?," *Journal of Biological Chemistry* 287 (2012): 1642–1648.

13. C. M.-F. de la Cámara, D. Salom, M. D. Sequedo, et al., "Altered Antioxidant-Oxidant Status in the Aqueous Humor and Peripheral Blood of Patients With Retinitis Pigmentosa," *PLoS One* 8 (2013): e74223.

14. N. G. Bazan and E. B. Rodriguez de Turco, "Review: Pharmacological Manipulation of Docosahexaenoic-Phospholipid Biosynthesis in Photoreceptor Cells: Implications in Retinal Degeneration," *Journal of Ocular Pharmacology and Therapeutics* 10 (1994): 591–604.

15. A. Catala, "Lipid Peroxidation of Membrane Phospholipids in the Vertebrate Retina," *Frontiers in Bioscience (Scholar Edition)* 3 (2011): 52–60.

16. K. Komeima, B. S. Rogers, L. Lu, and P. A. Campochiaro, "Antioxidants Reduce Cone Cell Death in a Model of Retinitis Pigmentosa," *Proceedings of the National Academy of Sciences of the United States of America* 103 (2006): 11300–11305.

17. J. Shen, X. Yang, A. Dong, et al., "Oxidative Damage Is a Potential Cause of Cone Cell Death in Retinitis Pigmentosa," *Journal of Cellular Physiology* 203 (2005): 457–464.

18. D.-Y. Yu, S. Cringle, K. Valter, N. Walsh, D. Lee, and J. Stone, "Photoreceptor Death, Trophic Factor Expression, Retinal Oxygen Status, and Photoreceptor Function in the P23H Rat," *Investigative Ophthalmology & Visual Science* 45 (2004): 2013–2019.

19. C. Punzo, K. Kornacker, and C. L. Cepko, "Stimulation of the Insulin/mTOR Pathway Delays Cone Death in a Mouse Model of Retinitis Pigmentosa," *Nature Neuroscience* 12 (2009): 44–52.

20. K. S. Park, C. L. Xu, X. Cui, and S. H. Tsang, "Reprogramming the Metabolome Rescues Retinal Degeneration," *Cellular and Molecular Life Sciences* 75 (2018): 1559–1566.

21. A. Venkatesh, S. Ma, Y. Z. Le, M. N. Hall, M. A. Rüegg, and C. Punzo, "Activated mTORC1 Promotes Long-Term Cone Survival in Retinitis Pigmentosa Mice," *Journal of Clinical Investigation* 125 (2015): 1446–1458.

22. A. Swarup, I. S. Samuels, B. A. Bell, et al., "Modulating GLUT1 Expression in Retinal Pigment Epithelium Decreases Glucose Levels in the Retina: Impact on Photoreceptors and Müller Glial Cells," *American Journal of Physiology. Cell Physiology* 316 (2019): C121–C133.

23. A. B. Wegrzyn, K. Herzog, A. Gerding, et al., "Fibroblast-Specific Genome-Scale Modelling Predicts an Imbalance in Amino Acid Metabolism in Refsum Disease," *FEBS Journal* 287 (2020): 5096–5113.

24. A. Luodan, T. Zou, J. He, et al., "Rescue of Retinal Degeneration in rd1 Mice by Intravitreally Injected Metformin," *Frontiers in Molecular Neuroscience* 12 (2019): 102.

25. D. Athanasiou, M. Aguila, C. A. Opefi, et al., "Rescue of Mutant Rhodopsin Traffic by Metformin-Induced AMPK Activation Accelerates Photoreceptor Degeneration," *Human Molecular Genetics* 26 (2017): 305–319.

26. E. Zhang, J. Ryu, S. R. Levi, et al., "PKM2 Ablation Enhanced Retinal Function and Survival in a Preclinical Model of Retinitis Pigmentosa," *Mammalian Genome* 31 (2020): 77–85.

27. R. S. Molday and O. L. Moritz, "Photoreceptors at a Glance," *Journal of Cell Science* 128 (2015): 4039–4045.

28. C. Hamel, "Retinitis Pigmentosa," *Orphanet Journal of Rare Diseases* 1 (2006): 40.

29. E. R. Weiss, S. Osawa, Y. Xiong, et al., "Broad Spectrum Metabolomics for Detection of Abnormal Metabolic Pathways in a Mouse Model for Retinitis Pigmentosa," *Experimental Eye Research* 184 (2019): 135–145.

30. A. B. Montaser, F. Gao, D. Peters, et al., "Retinal Proteome Profiling of Inherited Retinal Degeneration Across Three Different Mouse Models Suggests Common Drug Targets in Retinitis Pigmentosa," *Molecular & Cellular Proteomics* 23 (2024): 100855.

31. H. Gu, P. Jasbi, J. Patterson, and Y. Jin, "Enhanced Detection of Short-Chain Fatty Acids Using Gas Chromatography Mass Spectrometry," *Current Protocols* 1 (2021): e177.

32. P. Jasbi, D. Wang, S. L. Cheng, et al., "Breast Cancer Detection Using Targeted Plasma Metabolomics," *Journal of Chromatography B* 1105 (2019): 26–37.

33. H. Barrong, H. Coven, A. Lish, S. N. Fessler, P. Jasbi, and C. S. Johnston, "Daily Vinegar Ingestion Improves Depression and Enhances Niacin Metabolism in Overweight Adults: A Randomized Controlled Trial," *Nutrients* 16 (2024): 2305.

34. H. He, T. Pan, X. Shi, et al., "An Integrative Cellular Metabolomic Study Reveals Downregulated Tricarboxylic Acid Cycle and Potential Biomarkers Induced by Tetrabromobisphenol A in Human Lung A549 Cells," *Environmental Toxicology* 38 (2023): 7–16.

35. L. W. Sumner, A. Amberg, D. Barrett, et al., "Proposed Minimum Reporting Standards for Chemical Analysis," *Metabolomics* 3 (2007): 211–221.

36. M. Sud, E. Fahy, D. Cotter, et al., "Metabolomics Workbench: An International Repository for Metabolomics Data and Metadata, Metabolite Standards, Protocols, Tutorials and Training, and Analysis Tools," *Nucleic Acids Research* 44 (2016): D463–D470.

37. Z. Pang, J. Chong, G. Zhou, et al., "MetaboAnalyst 5.0: Narrowing the Gap Between Raw Spectra and Functional Insights," *Nucleic Acids Research* 49 (2021): W388–W396.

38. J. Xia and D. S. Wishart, "Web-Based Inference of Biological Patterns, Functions and Pathways From Metabolomic Data Using MetaboAnalyst," *Nature Protocols* 6 (2011): 743–760.

39. J. Xia and D. S. Wishart, "Metabolomic Data Processing, Analysis, and Interpretation Using MetaboAnalyst," *Current Protocols in Bioinformatics* 34 (2011): 14.10.1–14.10.48.

40. L. Eriksson, P. L. Andersson, E. Johansson, and M. Tysklind, "Megavariate Analysis of Environmental QSAR Data. Part I—A Basic Framework Founded on Principal Component Analysis (PCA), Partial Least Squares (PLS), and Statistical Molecular Design (SMD)," *Molecular Diversity* 10 (2006): 169–186.

41. Y. Benjamini and Y. Hochberg, "Controlling the False Discovery Rate: A Practical and Powerful Approach to Multiple Testing," *Journal of the Royal Statistical Society. Series B (Methodological)* 57 (1995): 289–300.

42. E. Saccenti, H. C. J. Hoefsloot, A. K. Smilde, J. A. Westerhuis, and M. M. W. B. Hendriks, "Reflections on Univariate and Multivariate Analysis of Metabolomics Data," *Metabolomics* 10 (2014): 361–374.

43. M. Vinaixa, S. Samino, I. Saez, J. Duran, J. J. Guinovart, and O. Yanes, "A Guideline to Univariate Statistical Analysis for LC/MS-Based Untargeted Metabolomics-Derived Data," *Metabolites* 2 (2012): 775–795.

44. S. Wold, M. Sjöström, and L. Eriksson, "PLS-Regression: A Basic Tool of Chemometrics," *Chemometrics and Intelligent Laboratory Systems* 58 (2001): 109–130.

45. W. E. Johnson, C. Li, and A. Rabinovic, "Adjusting Batch Effects in Microarray Expression Data Using Empirical Bayes Methods," *Biostatistics* 8 (2007): 118–127.

46. A. Frolkis, C. Knox, E. Lim, et al., "SMPDB: The Small Molecule Pathway Database," *Nucleic Acids Research* 38 (2010): D480–D487.

47. T. Jewison, Y. Su, F. M. Disfany, et al., "SMPDB 2.0: Big Improvements to the Small Molecule Pathway Database," *Nucleic Acids Research* 42 (2014): D478–D484.

48. J. Xia and D. S. Wishart, "MSEA: A Web-Based Tool to Identify Biologically Meaningful Patterns in Quantitative Metabolomic Data," *Nucleic Acids Research* 38 (2010): W71–W77.

49. S. Li, Y. Park, S. Duraisingham, et al., "Predicting Network Activity From High Throughput Metabolomics," *PLoS Computational Biology* 9 (2013): e1003123.

50. A. Subramanian, P. Tamayo, V. K. Mootha, et al., "Gene Set Enrichment Analysis: A Knowledge-Based Approach for Interpreting Genome-Wide Expression Profiles," *Proceedings of the National Academy of Sciences* 102 (2005): 15545–15550.

51. V. K. Mootha, C. M. Lindgren, K.-F. Eriksson, et al., "PGC-1α-Responsive Genes Involved in Oxidative Phosphorylation Are Coordinately Downregulated in Human Diabetes," *Nature Genetics* 34 (2003): 267–273.

52. M. Kanehisa and S. Goto, "KEGG: Kyoto Encyclopedia of Genes and Genomes," *Nucleic Acids Research* 28 (2000): 27–30.

53. M. Kanehisa, S. Goto, M. Hattori, et al., "From Genomics to Chemical Genomics: New Developments in KEGG," *Nucleic Acids Research* 34 (2006): D354–D357.

54. L. Xiang, Q.-L. Yang, B.-T. Xie, et al., "Dysregulated Arginine Metabolism Is Linked to Retinal Degeneration in Cep250 Knockout Mice," *Investigative Ophthalmology & Visual Science* 64 (2023): 2.

55. J. G. Dickhout, R. E. Carlisle, D. E. Jerome, et al., "Integrated Stress Response Modulates Cellular Redox State via Induction of Cystathionine γ-Lyase: Cross-Talk Between Integrated Stress Response and Thiol Metabolism," *Journal of Biological Chemistry* 287 (2012): 7603–7614.

56. X. Li and H.-S. Zhang, "Amino Acid Metabolism, Redox Balance and Epigenetic Regulation in Cancer," *FEBS Journal* 291 (2024): 412–429.

57. K. Kim, L. A. Safarta, W.-C. J. Chiang, J. A. Coppinger, E.-J. Lee, and J. H. Lin, "Network Biology Analysis of P23H Rhodopsin Interactome Identifies Protein and mRNA Quality Control Mechanisms," *Scientific Reports* 12 (2022): 17405.

58. Y. Chen, L. Zizmare, V. Calbiague, et al., "Retinal Metabolism: Evidence for Uncoupling of Glycolysis and Oxidative Phosphorylation via Cori-, Cahill-, and Mini-Krebs-Cycle," *eLife* 12 (2024): RP91141.

59. B. V. Bui, R. G. Hu, M. L. Acosta, P. Donaldson, A. J. Vingrys, and M. Kalloniatis, "Glutamate Metabolic Pathways and Retinal Function," *Journal of Neurochemistry* 111 (2009): 589–599.

60. V. Sánchez-Vallejo, S. Benlloch-Navarro, L. Trachsel-Moncho, et al., "Alterations in Glutamate Cysteine Ligase Content in the Retina of Two Retinitis Pigmentosa Animal Models," *Free Radical Biology and Medicine* 96 (2016): 245–254.

61. A. N. Lane and T. W.-M. Fan, "Regulation of Mammalian Nucleotide Metabolism and Biosynthesis," *Nucleic Acids Research* 43 (2015): 2466–2485.

62. L. Wan, J. Li, W.-B. Chen, and G.-Q. Wu, "Beneficial Effects of Protocatechuic Acid on Diabetic Retinopathy in Streptozocin-Induced Diabetic Rats," *International Journal of Ophthalmology* 16 (2023): 855–862.

63. C. E. Bowman, S. Rodriguez, E. S. Selen Alpergin, et al., "The Mammalian Malonyl-CoA Synthetase ACSF3 Is Required for Mitochondrial Protein Malonylation and Metabolic Efficiency," *Cell Chemical Biology* 24 (2017): 673–684.e4.

64. Z. Wang, X. Pan, D. Wang, et al., "Protective Effects of Protocatechuic Acid on Retinal Ganglion Cells From Oxidative Damage Induced by H_2O_2," *Neurological Research* 37 (2015): 159–166.

65. P.-H. Gabrielle, "Lipid Metabolism and Retinal Diseases," *Acta Ophthalmologica* 100, no. Suppl 269 (2022): 3–43.

66. S. Fatima, X. Hu, R.-H. Gong, et al., "Palmitic Acid Is an Intracellular Signaling Molecule Involved in Disease Development," *Cellular and Molecular Life Sciences* 76 (2019): 2547–2557.

67. T. TeSlaa, C. R. Bartman, C. S. R. Jankowski, et al., "The Source of Glycolytic Intermediates in Mammalian Tissues," *Cell Metabolism* 33 (2021): 367–378.e5.

68. J. R. Chao, K. Knight, A. L. Engel, et al., "Human Retinal Pigment Epithelial Cells Prefer Proline as a Nutrient and Transport Metabolic Intermediates to the Retinal Side," *Journal of Biological Chemistry* 292 (2017): 12895–12905.

69. J. Du, S. Zhu, R. R. Lim, and J. R. Chao, "Proline Metabolism and Transport in Retinal Health and Disease," *Amino Acids* 53 (2021): 1789–1806.

70. R. S. Schibalski, A. S. Shulha, B. P. Tsao, O. Palygin, and D. V. Ilatovskaya, "The Role of Polyamine Metabolism in Cellular Function and Physiology," *American Journal of Physiology-Cell Physiology* 327 (2024): C341–C356.

71. K. J. Wert, A. Rowe, and R. Gordillo, "Dysregulation of Tricarboxylic Acid (TCA) Cycle Activity and Lipid Metabolism in Preclinical Models of Retinitis Pigmentosa," *Investigative Ophthalmology & Visual Science* 63 (2022): 874.

72. A. A. Rowe, P. D. Patel, R. Gordillo, and K. J. Wert, "Replenishment of TCA Cycle Intermediates Provides Photoreceptor Resilience Against Neurodegeneration During Progression of Retinitis Pigmentosa," *JCI Insight* 6 (2021): e150898.

73. S. Zarrella, M. R. Miranda, V. Covelli, et al., "Endoplasmic Reticulum Stress and Its Role in Metabolic Reprogramming of Cancer," *Metabolites* 15 (2025): 221.

74. N. Ho, C. Xu, and G. Thibault, "From the Unfolded Protein Response to Metabolic Diseases—Lipids Under the Spotlight," *Journal of Cell Science* 131 (2018): jcs199307.

75. D. Senft and Z. A. Ronai, "UPR, Autophagy, and Mitochondria Crosstalk Underlies the ER Stress Response," *Trends in Biochemical Sciences* 40 (2015): 141–148.

76. M. G. Metcalf, R. Higuchi-Sanabria, G. Garcia, C. K. Tsui, and A. Dillin, "Beyond the Cell Factory: Homeostatic Regulation of and by the UPR^{ER}," *Science Advances* 6 (2020): eabb9614.

77. M. T. T. Wong-Riley, "Energy Metabolism of the Visual System," *Eye and Brain* 2 (2010): 99–116.

78. D.-Y. Yu and S. J. Cringle, "Oxygen Distribution and Consumption Within the Retina in Vascularised and Avascular Retinas and in Animal Models of Retinal Disease," *Progress in Retinal and Eye Research* 20 (2001): 175–208.

79. J. Du, A. Rountree, W. M. Cleghorn, et al., "Phototransduction Influences Metabolic Flux and Nucleotide Metabolism in Mouse Retina," *Journal of Biological Chemistry* 291 (2016): 4698–4710.

80. Y. Chinchore, T. Begaj, D. Wu, E. Drokhlyansky, and C. L. Cepko, "Glycolytic Reliance Promotes Anabolism in Photoreceptors," *eLife* 6 (2017): e25946.

81. J. B. Hurley, K. J. Lindsay, and J. Du, "Glucose, Lactate, and Shuttling of Metabolites in Vertebrate Retinas," *Annual Review of Vision Science* 1 (2015): 285–308.

82. H. P. Harding, Y. Zhang, H. Zeng, et al., "An Integrated Stress Response Regulates Amino Acid Metabolism and Resistance to Oxidative Stress," *Molecular Cell* 11 (2003): 619–633.

83. J. Han, S. H. Back, J. Hur, et al., "ER-Stress-Induced Transcriptional Regulation Increases Protein Synthesis Leading to Cell Death," *Nature Cell Biology* 15 (2013): 481–490.

84. M. Emmett, "Acetaminophen Toxicity and 5-Oxoproline (Pyroglutamic Acid)," *Clinical Journal of the American Society of Nephrology* 9 (2014): 191–200.

85. J. R. Cubillos-Ruiz, S. E. Bettigole, and L. H. Glimcher, "Tumorigenic and Immunosuppressive Effects of Endoplasmic Reticulum Stress in Cancer," *Cell* 168 (2017): 692–706.

86. K. R. Bhattarai, T. A. Riaz, H.-R. Kim, and H.-J. Chae, "The Aftermath of the Interplay Between the Endoplasmic Reticulum Stress Response and Redox Signaling," *Frontiers in Cell and Developmental Biology* 9 (2021): 684793.

87. A. Almanza, K. Mnich, A. Blomme, et al., "Metabolites and the ER Stress Response: A Systems Perspective," *Metabolites* 15 (2025): 221.

88. I. M. N. Wortel, L. T. van der Meer, M. S. Kilberg, and F. N. van Leeuwen, "Surviving Stress: Modulation of ATF4-Mediated Stress Responses in Normal and Malignant Cells," *Trends in Endocrinology and Metabolism* 28 (2017): 794–806.

89. D. Athanasiou, M. Aguila, J. Bellingham, N. Kanuga, P. Adamson, and M. E. Cheetham, "The Role of the ER Stress-Response Protein PERK in Rhodopsin Retinitis Pigmentosa," *Human Molecular Genetics* 26 (2017): 4896–4905.

90. F. Fayolle, J.-P. Vandecasteele, and F. Monot, "Microbial Degradation and Fate in the Environment of Methyl Tert-Butyl Ether and Related Fuel Oxygenates," *Applied Microbiology and Biotechnology* 56 (2001): 339–349.

91. C. R. Canez and L. Li, "Studies of Labware Contamination During Lipid Extraction in Mass Spectrometry-Based Lipidome Analysis," *Analytical Chemistry* 96 (2024): 3544–3552.

92. O. F. Kuzu, L. J. T. Granerud, and F. Saatcioglu, "Navigating the Landscape of Protein Folding and Proteostasis: From Molecular Chaperones to Therapeutic Innovations," *Signal Transduction and Targeted Therapy* 10 (2025): 358.

93. T. W. Kensler, N. Wakabayashi, and S. Biswal, "Cell Survival Responses to Environmental Stresses via the Keap1-Nrf2-ARE Pathway," *Annual Review of Pharmacology and Toxicology* 47 (2007): 89–116.

94. A. Cuadrado, A. I. Rojo, G. Wells, et al., "Therapeutic Targeting of the NRF2 and KEAP1 Partnership in Chronic Diseases," *Nature Reviews Drug Discovery* 18 (2019): 295–317.

95. R. M. Chin, X. Fu, M. Y. Pai, et al., "The Metabolite α-Ketoglutarate Extends Lifespan by Inhibiting ATP Synthase and TOR," *Nature* 510 (2014): 397–401.

96. C. Sidrauski, D. Acosta-Alvear, A. Khoutorsky, et al., "Pharmacological Brake-Release of mRNA Translation Enhances Cognitive Memory," *eLife* 2 (2013): e00498.

97. C. Sidrauski, A. M. McGeachy, N. T. Ingolia, and P. Walter, "The Small Molecule ISRIB Reverses the Effects of eIF2α Phosphorylation on Translation and Stress Granule Assembly," *eLife* 4 (2015): e05033.

98. K. Pakos-Zebrucka, I. Koryga, K. Mnich, M. Ljujic, A. Samali, and A. M. Gorman, "The Integrated Stress Response," *EMBO Reports* 17 (2016): 1374–1395.

Supporting Information

Additional supporting information can be found online in the Supporting Information section. **Data S1:** fsb272130-sup-0001-DataS1.docx. **Table S1:** In-house GC–MS spectral library of 126 authentic chemical standards used for metabolite identification at MSI Level 1 [35]. All entries were verified against authentic standards run under identical GC–MS conditions (Methods). KEGG identifiers were resolved via PubChem cross-references (122 entries) and MetaboAnalyst name-based mapping (4 entries). MSI Level 1 identification is achieved by co-elution of an unknown with the authentic standard and matching electron-impact (EI) mass spectrum. Quantifier ion is the base peak of the EI spectrum under the conditions described; full EI spectra and all qualifier ions are deposited together with the raw data at the NIH Metabolomics Workbench. **Table S2:** Full list of metabolites compared between P23A and P23A/N2C/D282C across different experimental batches. **Table S3:** List of statistically significant metabolites with raw and log *p*-values for pairwise comparison. **Table S4:** Metabolite-level statistics and associated *p*-values, FDR, and pathway impacts. **Figure S1:** Boxplots of metabolite levels for WT, P23A and P23A/N2C/D282C. The bar plots display normalized values as means ± one standard deviation. Box plots show the interquartile range (25th to 75th percentiles), with whiskers extending to the 5th and 95th percentiles (Fold Change ≥ 1.0; raw p-value < 0.05). **Figure S2:** fsb272130-sup-0004-FigureS2.png. **Figure S3:** fsb272130-sup-0005-FigureS3.png.